UAB
Universitat Autònoma de Barcelona

High Resolution Ultrasound Platform for Screening of Infections in Serous Body Fluids: the Infant Meningitis Case

Manuel Navarrete Hernández

ADVERTIMENT. L'accés als continguts d'aquesta tesi doctoral i la seva utilització ha de respectar els drets de la persona autora. Pot ser utilitzada per a consulta o estudi personal, així com en activitats o materials d'investigació i docència en els termes establerts a l'art. 32 del Text Refós de la Llei de Propietat Intel·lectual (RDL 1/1996). Per altres utilitzacions es requereix l'autorització prèvia i expressa de la persona autora. En qualsevol cas, en la utilització dels seus continguts caldrà indicar de forma clara el nom i cognoms de la persona autora i el títol de la tesi doctoral. No s'autoritza la seva reproducció o altres formes d'explotació efectuades amb finalitats de lucre ni la seva comunicació pública des d'un lloc aliè al servei TDX. Tampoc s'autoritza la presentació del seu contingut en una finestra o marc aliè a TDX (framing). Aquesta reserva de drets afecta tant als continguts de la tesi com als seus resums i índexs.

ADVERTENCIA. El acceso a los contenidos de esta tesis doctoral y su utilización debe respetar los derechos de la persona autora. Puede ser utilizada para consulta o estudio personal, así como en actividades o materiales de investigación y docencia en los términos establecidos en el art. 32 del Texto Refundido de la Ley de Propiedad Intelectual (RDL 1/1996). Para otros usos se requiere la autorización previa y expresa de la persona autora. En cualquier caso, en la utilización de sus contenidos se deberá indicar de forma clara el nombre y apellidos de la persona autora y el título de la tesis doctoral. No se autoriza su reproducción u otras formas de explotación efectuadas con fines lucrativos ni su comunicación pública desde un sitio ajeno al servicio TDR. Tampoco se autoriza la presentación de su contenido en una ventana o marco ajeno a TDR (framing). Esta reserva de derechos afecta tanto al contenido de la tesis como a sus resúmenes e índices.

WARNING. The access to the contents of this doctoral thesis and its use must respect the rights of the author. It can be used for reference or private study, as well as research and learning activities or materials in the terms established by the 32nd article of the Spanish Consolidated Copyright Act (RDL 1/1996). Express and previous authorization of the author is required for any other uses. In any case, when using its content, full name of the author and title of the thesis must be clearly indicated. Reproduction or other forms of for profit use or public communication from outside TDX service is not allowed. Presentation of its content in a window or frame external to TDX (framing) is not authorized either. These rights affect both the content of the thesis and its abstracts and indexes.

UNIVERSITAT AUTÒNOMA DE BARCELONA

PHD PROGRAM IN ELECTRONIC AND TELECOMMUNICATION ENGINEERING

High Resolution Ultrasound Platform for Screening of Infections in Serous Body Fluids: the Infant Meningitis Case

---

Author:
Manuel NAVARRETE HERNÁNDEZ

Supervisors:
Dr. Jordi CARRABINA BORDOLL,
DR. DAVID CASTELLS RUFAS

A thesis submitted in fulfillment of the requirements for the degree of Doctor of Philosophy

in the

Department of Microelectronics and Electronic Systems

June 14, 2024

Declaration of Authorship

I, Manuel NAVARRETE HERNÁNDEZ, declare that this thesis titled, "High Resolution Ultrasound Platform for Screening of Infections in Serous Body Fluids: the Infant Meningitis Case" and the work presented in it are my own. I confirm that:

- This work was done wholly or mainly while in candidature for a research degree at this University.
- Where any part of this thesis has previously been submitted for a degree or any other qualification at this University or any other institution, this has been clearly stated.
- Where I have consulted the published work of others, this is always clearly attributed.
- Where I have quoted from the work of others, the source is always given. With the exception of such quotations, this thesis is entirely my own work.
- I have acknowledged all main sources of help.
- Where the thesis is based on work done by myself jointly with others, I have made clear exactly what was done by others and what I have contributed myself.

Signed: NAVARRETE HERNANDEZ MANUEL - 60140186Q Firmado digitalmente por NAVARRETE HERNANDEZ MANUEL Fecha: 2024.06.14 05:49:22 +02'00'

Date:

"The best way to predict the future is to create it."

Peter Drucker

UNIVERSITAT AUTÒNOMA DE BARCELONA

Abstract

Engineering School
Department of Microelectronics and Electronic Systems

Doctor of Philosophy

High Resolution Ultrasound Platform for Screening of Infections in Serous Body Fluids: the Infant Meningitis Case

by Manuel NAVARRETE HERNÁNDEZ

Infant meningitis remains a severe burden on global health, particularly for young infants. The urgency to solve this problem demands alternative solutions that can be widely applied. The assessment of white blood cell (WBC) concentration in the cerebrospinal fluid (CSF) is key to the diagnosis of meningitis. Ultrasound emerges as an ideal technology for such application, due to its low cost, portability, and safety. However, conventional ultrasound techniques are limited in spatial resolution to detect WBCs in the CSF.

This thesis presents the research and development process of a portable device that uses high-resolution ultrasound to evaluate WBC concentration in the CSF through the fontanelle of neonates and young infants. This novel approach aims to provide a non-invasive alternative to the traditional diagnostic methods for infant meningitis, offering a rapid and accessible screening tool. The developed platform employs a 20 MHz focused transducer, significantly enhancing spatial resolution and enabling the detection of the backscatter signals from microscopic WBCs. The whole system was built around a custom probe that allows the transducer to be mechanically controlled to map the area of interest in the CSF.

Hardware and software components were carefully integrated into an artificial intelligence (AI)-powered platform capable of accurate imaging and CSF analysis. *In vitro* evaluation and optimization process were essential to achieve high-quality images while complying with safety guidelines. Experiments using a tube phantom through neonatal fontanelle with 7-μm particles suspensions under different concentrations provided essential information on particle dynamics relevant to the diagnosis of meningitis. The developed system allows the acquisition of high-resolution images that provide excellent clarity and detail. In addition, the high acquisition rate enables to track the resulting particle pattern in the images with lateral coherence.

An Deep Learning (DL) model was deployed into the platform to classify patients based on CSF patterns according to WBC concentrations. This tool facilitates prompt treatment initiation if diagnostic thresholds are exceeded. Optimized for the platform-specific hardware, the algorithms integrated into the device ensure fast on-site analysis in a matter of minutes.

Clinical trials in Spain, Morocco, and Mozambique have yielded promising preliminary results that demonstrate the potential of the platform to support the diagnosis of meningitis. This thesis establishes a robust methodology for immediate and accurate CSF analysis, advancing the diagnosis of infant meningitis through a well-optimized and rigorously evaluated high

resolution ultrasound platform.

Acknowledgements

I am deeply grateful to all those who have supported and guided me along the way to complete this thesis. First, I would like to express my sincere gratitude to my thesis directors, Jordi Carrabina Bordoll and David Castells Rufas, for their continuous support, invaluable guidance, and constructive feedback. Your expertise and encouragement have been instrumental in shaping this work and bringing it to successful completion.

Altogether, I would like to thank Javier Jiménez González, CEO at Kriba and my supervisor on the company side, where I have developed a large extent of my research. Thank you very much for the opportunity, for believing in this great project and for taking it forward. Your support and trust have decisively influenced in all the work that is now bearing fruit.

I extend my sincere gratitude to Hassane Baghdad Kichou for sharing his invaluable experience in the field of ultrasound and electronics in general. Your guidance has marked the path taken at many stages of this thesis.

I am also profoundly thankful to my colleagues and friends at Kriba. Your willingness to help at all times has made this trip a rewarding experience. A special mention goes to Guillermo Navarro Patrón, Ramon Serrano Deulonder, Fabião Santos Abreu, Beatrice Jobst, Francesc Carandell Verdaguer, Rita Quesada Diez and Valentine Pironneau for their constant support and assistance. I would also like to thank my colleagues at UAB, Ashkan Rezaee and Marc Codina Barberà for their support during the first stage of this thesis.

But mainly, to my family. To my parents, Hilda and Ernesto, thank you for your endless love, support and patience. To my partner, Jessica, you have been a source of immense strength and motivation. To my siblings, Carmen and Andrés, for their constant support for everything. Special thanks to my uncles and aunts, Alfredo and María as well as Fidel and Igone, for always being present along the way.

To everyone who has contributed to this thesis in one way or another, I am deeply grateful.

Contents

Declaration of Authorship iii

Abstract viii

Acknowledgements xi

1 Introduction 1
- 1.1 Traditional methods to diagnose meningitis . . . 3
- 1.2 Challenges in CSF WBC detection through the fontanelle of infants using conventional ultrasound imaging . . . 5
- 1.3 Methods to improve the resolution of ultrasound imaging . . 7
- 1.4 About this thesis . . . 10

2 Fundamentals of ultrasound 13
- 2.1 Physical characteristics of sound . . . 13
- 2.2 Techniques of ultrasound imaging . . . 15
- 2.3 Transducers . . . 17
- 2.4 Propagation in Tissues . . . 18
- 2.5 Bioeffects of ultrasound . . . 21

3 System design 23
- 3.1 System requirements . . . 23
- 3.2 Related design choices . . . 26
- 3.3 System architecture . . . 30
- 3.4 Methodology and tools . . . 32

4 Software implementation and verification 37
- 4.1 Probe control . . . 37
- 4.2 Inter-module connectivity . . . 39
- 4.3 Ultrasound data management . . . 44
- 4.4 AI at the edge . . . 53

5 Tests and results **55**
5.1 Experimental setup 55
5.2 Optimization of ultrasound configuration 57
5.3 Evaluation of system resolution 62
5.4 On-device evaluation of CSF classification according to WBC concentration 66

6 Conclusions and future directions **71**
6.1 Conclusions 71
6.2 Future directions 73

A Application Graphical User Interface (GUI) **75**

Bibliography **77**

List of Figures

1.1 Cross-sectional cut of the proposed hand-held ultrasonic device to detect meningitis. 11

2.1 Traditional ultrasound techniques are based on the echo of the tissues due to the variation of their acoustic impedance. The echoes are very strong at first, and then decrease rapidly as the time-of-flight increases. 16
2.2 Reflection and refraction of ultrasound beams. 19

3.1 Pulse–echo impulse response and spectrum of the selected 20-MHz transducer. 28
3.2 Block diagram of the system 30
3.3 (a) Surface sensed during image generation; (b) Acquired image as shown on display. 32
3.4 System design flow 34

4.1 Block diagram of each stepper motor control. 38
4.2 Block diagram of the probe-base Universal Asynchronous Receiver-Transmitter (UART) communication using On–Off Keying (OOK) modulation over the Direct Current (DC) power line. 39
4.3 Example of probe-base UART communication using OOK modulation over the DC power line. The following signals are shown highlighted in color: (yellow) UART communication signal transmitted; (blue) UART communication signal received and; (green) carrier. 41
4.4 Multi-threading scheme for the Central Processing Unit (CPU) application 42
4.5 Frame exchange routine 42
4.6 Interaction overview diagram between system modules. . . . 43
4.7 Control chain for data acquisition from the pulser-receiver: (1) open connection, (2) initial configuration, (3) data acquisition and (4) close connection 44

4.8 Control block for acquisitions triggered by software, consisting of: (1) *run* order transmission, (2) User Datagram Protocol (UDP) data reception, (3) frame decoding and (4) image composition. 45
4.9 (1) Misalignment between the pulse train that triggers the scan motor steps (yellow waveform) and the firing events of each pulse-echo process (purple waveform). (2) Firing events are not equally spaced in time. 46
4.10 Synchronism between the pulse train that triggers the scan motor steps (yellow waveform) and the firing events of each pulse-echo process (purple waveform). 47
4.11 (a) Pulse amplitude = -50 V; (b) Pulse amplitude = -75 V; (c) Pulse amplitude = -100 V 49
4.12 (a) Pulse width = 20 ns; (b) Pulse width = 25 ns; (c) Pulse width = 30 ns 49
4.13 (a) Pulses number = 1; (b) Pulses number = 2; (c) Pulses number = 3 49
4.14 (a) Pulse-Repetition Frequency (PRF) = 10 kHz; (b) PRF = 15 kHz; (c) PRF = 20 kHz 49
4.15 Memory space allocated for filter coefficients in the pulser-receiver. 50
4.16 Receiver configuration to select the acquisition range of the returning echo, from which each A-scan (scan line) is obtained. This configuration ensures that the focal zone (yellow square) lies in the center of the acquisition range. Each frame is created from 736 scan lines acquired consecutively every 1 ms. 52
4.17 (a) HR scan path vs HHR scan path; (b) HR img vs HHR img. 52

5.1 Experimental setup composed of: (1) ultrasound probe, (2) bracket, (3) sample container, (4) elevating platform, (5) base module, and (6) external monitor. 56
5.2 Measurement of the pulse–echo impulse response and spectrum of the 20-MHz transducer. 56
5.3 B-mode images (video-mode) obtained when the transducer is excited with: (a) -50 V, (b) -75 V and, (c) -100 V single-squared pulses of 25 ns wide. Echo signals are amplified 32 dB before being input into the receiving stage. A second amplification gain in the range 35 dB is further applied. 58

5.4 B-mode images (video-mode) obtained by averaging returning echoes over (a) 2, (b) 4, and, (c) 8 transmission cycles to get each A-scan that form the image, using a 20 KHz PRF. The transducer is excited with a -75 V single-squared pulses of 25 ns wide. 59
5.5 B-mode image obtained by averaging returning echoes over 4 transmission cycles to get every A-scan that form the image, using a 27 kHz PRF. The transducer is excited with a -75 V, 25 ns wide single-squared pulses. 60
5.6 Comparison of magnitude frequency response of designed Finite Impulse Response (FIR) bandpass (10 MHz - 30 MHz) filters based on: (1) windows (Hamming), (2) frequency sampling, (3) Parks–McClellan transformation and, (4) Least-squares. . . 61
5.7 Radio Frequency (RF) signal filtered by a least-squares linear-phase FIR filter between 10 and 30 MHz. 61
5.8 Thermal Index (TI) (a) and Mechanical Index (MI) (b) measurements (marked -•-) according to pulse amplitude configurations of -50 V and -75 V. New data points (marked -○-) corresponding to -100 V are obtained by linear interpolation. Red lines indicate the Food and Drug Administration (FDA) recommended limits of TI < 0.7 and MI < 0.9. 62
5.9 Detail of the High Resolution (HR) B-mode images (video-mode) obtained with setup 1 on 7–μm particles suspension under 7-, 19-, 69- and 646–pp/μL concentrations, respectively from left to right. 64
5.10 Detail of the Higher Resolution (HHR) B-mode images (video-mode) obtained with setup 1 on 7–μm particles suspension under 7-, 19-, 69- and 646–pp/μL concentrations, respectively from left to right. 64
5.11 Detail of the HR B-mode images (video-mode) obtained with setup 2 on 7–μm particles suspension under 7-, 19-, 69- and 646–pp/μL concentrations, respectively from left to right. . . . 65
5.12 Detail of the HHR B-mode images (video-mode) obtained with setup 2 on 7–μm particles suspension under 7-, 19-, 69- and 646–pp/μL concentrations, respectively from left to right. . . . 65

5.13 Difference on the pressure effect of the ultrasound beam on the speed of a particle depending on its location: (a) above the focal area, (b) in the focal area, and (c) below the focal area. This location dependent pressure effect creates a sigmoid shaped trace on the particle trajectories when multiple scans are consecutively shot without moving the scanner head (M-mode, extreme case) (d). 66
5.14 Example of the probability distribution of the 18 images acquired for two patients. According to the ground truth, controls are labeled in blue and meningitis cases in orange. Each dot shows the probability of each image of belonging to the control class (X axis) versus belonging to the meningitis class (Y axis). The crosses indicate the final classification (median probability) for each patient. 67
5.15 Performance comparison when running inference of the classification model on (a) NVIDIA GeForce RTX 3090 using CUDA vs (b) Graphics Processing Unit (GPU) accelerator of the Jetson Nano using TensorRT. 68

A.1 Application GUI from which the system can be controlled in an advanced way, compared to the Touch Display, which is more limited. This GUI is composed of the following elements: (1) patient ID indicator, (2) HHR zone control, (3) focus control, (4) view control, (5) corresponding view, (6) start/end operation control, (7) connected modules indicator, (8) ultrasound parameters configuration panel. This specific case corresponds to the Test view, from where the HHR B-mode image can be observed. 75
A.2 Evaluation view (1) of the application GUI, from where the individual scan lines (A-scans) can be analyzed in the time (2) and frequency domain (magnitude (3) and phase (4)). 76

List of Tables

2.1 Frequency Spectrum of Sound 14
2.2 Speed of sound in various media. Table extracted from [47] . . 15

3.1 Characteristics of the selected transducer 27

5.1 Initial configuration of acquisitions. 57
5.2 Ultrasound configuration adapted for the meningitis application in which images are optimally displayed while complying with the regulatory safety limits. 63
5.3 Performance of the classification model of CSF patterns according to the WBC concentration. 68

List of Abbreviations

2D two-dimension

3D three-dimension

ADC Analog-to-Digital Converter

AI artificial intelligence

ALARA as low as reasonably achievable

API Application Programming Interface

ASK Amplitude-Shift Keying

BBB blood brain barrier

CUS cranial ultrasound

CPU Central Processing Unit

CSF cerebrospinal fluid

CT Computed Tomography

CTP Capacitive Touch Panel

DAC Digital-to-Analog Converter

DC Direct Current

DL Deep Learning

DSP Digital Signal Processing

FDA Food and Drug Administration

FIR Finite Impulse Response

FPGA Field-Programmable Gate Array

FSM Finite State Machine

GPU Graphics Processing Unit

GUI Graphical User Interface

HHR Higher Resolution

HIV Human Immunodeficiency Virus

HPC high-performance computing

HR High Resolution

IDE Integrated Development Environment

LCD Liquid-Crystal Display

LP lumbar puncture

MCU Microcontroller Unit

MI Mechanical Index

MRI Magnetic Resonance Imaging

NF Noise Figure

NN neural network

ONNX Open Neural Network Exchange

OOK On–Off Keying

PCC Pearson correlation coefficient

PRF Pulse-Repetition Frequency

PVA polyvinyl alcohol

PWM Pulse-Width Modulation

RF Radio Frequency

SDK Software Development Kit

SNR Signal-to-Noise Ratio

SPI Serial Peripheral Interface

SPL spatial pulse length

TCP Transmission Control Protocol

TFT Thin-Film-Transistor

TI Thermal Index

UBM Ultrasound Biomicroscopy

UDP User Datagram Protocol

UART Universal Asynchronous Receiver-Transmitter

WBC white blood cell

List of Symbols

a	distance	m
f	frequency	Hz
P	power	W
T	temperature	°C
t	time	s
V	volume	L

Dedicado a mi familia

Chapter 1

Introduction

Meningitis is a severe disease with a high mortality rate, often causing serious long-term complications. Meningitis refers to the inflammation of the meninges, the membranes covering the brain and spinal cord [1, 2]. It is identified through an abnormal number of white blood cell in the CSF [3]. Meningitis can be caused by bacteria, viruses, fungi, and less commonly parasites [4]. Bacterial meningitis is the most common dangerous type. Approximately 1 in 6 people who contract this type of meningitis die and 1 in 5 suffer serious complications [2]. Early diagnosis and corresponding treatment are critical to minimize mortality or sequelae among survivors.

Despite advances in diagnosis, treatment, and vaccination [5], meningitis remains a major global public-health challenge. In 2016, there were 2.82 million cases of meningitis worldwide, with 318000 related deaths (4.5 per 100,000 persons) [6]. The highest incidence of meningitis in the world is in sub-Saharan Africa, known as the African Meningitis Belt stretching from Ethiopia to Senegal [4, 7]. The incidence rates vary per country, with most recent rates varying from 0.7 to 0.9 per 100,000 per year in the United States and European countries, whereas studies from Africa describe incidence rates varying from 10 to 40 per 100,000 per year [3].

Traditional methods to diagnose meningitis typically involve a clinical examination followed by a lumbar puncture (LP). This procedure is considered the gold standard for diagnosing meningitis. Analysis of the CSF can reveal the presence of infection, by observing an increase in white blood cell, and other markers that help identify the cause and severity of meningitis. Other diagnostic methods, such as blood tests and imaging studies, may be used in conjunction with a lumbar puncture to support the diagnosis and guide treatment.

The access to all these tests and services is often insufficient in resource-poor countries, where the burden of meningitis is usually higher [8]. Specifically, lumbar punctures are less available, leading to increased rates of misdiagnosis, mortality and morbidity. In contrast, the incidence of the disease is low in most industrialized countries. However, the number of negative punctures is very high. This is because LP is the principal procedure used in clinical practice to screen for infant meningitis [9]. Routine lumbar punctures for screening for infant meningitis are negative in most cases, and results can often be delayed due to blood contamination.

Meningitis suspicion is challenging due to the nonspecific symptoms associated to the infection, such as fever, headache, neck stiffness among others that can also be caused by other diseases. Particularly, signs and symptoms are less noticeable in neonates and young infants. That is why clinical history and physical evaluation alone are generally insufficient to confirm or exclude the diagnosis. Lumbar puncture to draw a sample of CSF is an essential and systematic investigation by protocol in the suspected patient, but difficult to perform and potentially dangerous for a sick child.

Although meningitis can affect all ages, young children are most at risk. Particularly, infants under the age of 1 year are at a high risk for meningitis [10, 11], especially newborns in the first month of life, because their immune system is not fully developed [12]. Therefore, since they are most susceptible to infections, special attention should be paid to this age group.

All these challenges demand for practical solutions that enable alternative ways for direct mapping (*in vivo*) the CSF in infants. The assessment of WBC concentration in the CSF using minimally invasive or non-invasive approaches would provide valuable information while complementing the limitations of lumbar puncture or other invasive methods. Innocuous and non-invasive ultrasound has been used for the characterization of biological tissues and is presented as a suitable tool for the measurement of cell concentration in serous body fluids, specifically in the CSF [13, 14, 15, 16]. As usual in cranial ultrasound (CUS), images can be obtained through the anterior fontanelle of the neonate, to take advantage of this acoustic window [17, 18]. This way, the skull bone is avoided, which is the main obstacle for high resolution ultrasound brain imaging [19]. Such method has the potential to achieve real-time measurements while applying minimal stress to the patient under evaluation.

As a summary, this first chapter has started by bringing the spotlight on meningitis disease, as a global burden with devastating consequences for

people, especially young infants. In Section 1.1, traditional methods to diagnose meningitis are highlighted to understand the limitations of current techniques while providing a starting point on which to build a new alternative. Section 1.2 refers to the main challenges in CSF white blood cells detection using high-frequency ultrasound. Section 1.3, review the state-of-the-art methods for improving the resolution of ultrasound imaging and evaluate cell concentration in serous body fluids using ultrasound imaging. Finally, in Section 1.4, a promising new solution based on high frequency ultrasound imaging for early detection of infant meningitis is introduced as the main topic on which this thesis has been developed. In addition, the methodological aspects of the thesis are defined, specifying the motivation behind the work as well as the hypothesis and the objectives to be achieved.

1.1 Traditional methods to diagnose meningitis

Traditional methods to diagnose meningitis typically involve a combination of clinical evaluation, lumbar puncture, laboratory tests, and imaging studies.

1.1.1 Clinical evaluation

Clinical presentation of meningitis can vary depending on age and immune status of the patient, but also depends on the cause of the infection. Typical symptoms are fever, headache, stiff neck, and altered mental status, as well as nausea and vomiting [20]. Less common symptoms are seizures, coma and focal neurological deficits [2]. A check should be made of possible exposures, sexual history, drug abuse, vaccine records, contact with animals, past neurosurgical interventions and previous travel [21].

In adults, physical examination focuses on the identification of focal neurological deficits, altered mental status, meningeal irritation and, especially in meningococcal meningitis, distinctive skin lesions [4]. Clinical presentation in neonates and infants is more vague, with symptoms such as irritability, with or without fever, lethargy, or decreased oral intake [22].

Although useful in combination with other tests, clinical evaluation alone is not reliable in determining whether or not meningitis is present.

1.1.2 Lumbar puncture

Accurate diagnosis of meningitis requires the analysis of CSF, collected from the spinal canal via a lumbar puncture. This is the gold standard procedure for diagnosing meningitis. This procedure consist of inserting a needle into the patient's lower back to obtain a CSF sample for analysis. This analysis helps identify the presence of infectious agents like bacteria, viruses, and other abnormalities such as increased white blood cell concentration [23]. The WBC count in the CSF is a well-established marker for the diagnosis of infant meningitis. Meningitis is typically identified by means of a CSF pleocytosis [3]. The detection of a low (5-25 WBC/μL), but abnormal concentration of WBC raises clinical suspicion of meningitis infection [14]. If diagnostic WBC levels in the CSF are exceeded and meningitis infection is suspected, treatment must be started. Additional tests appropriate to the suspected etiology should be performed.

Performing lumbar punctures requires clinical experience, especially in young patients and neonates. It can produce adverse events such as apnea and desaturation in the sick newborn. Lumbar punctures can also be hemorrhagic or traumatic, with neonates being at greater risk [24]. In addition, the presence of blood complicates the laboratory analysis of CSF [25]. As an invasive technique that causes stress to the patient, it represents a major concern for caregivers [26].

1.1.3 Blood test

Blood test can help identify bacteria, viruses or other specific pathogens in the bloodstream, indicating a systemic infection. Other blood tests may be performed to assess overall health and identify inflammatory markers. These tests may include blood cultures, serum electrolytes levels, serum glucose, renal and liver function, and testing for Human Immunodeficiency Virus (HIV) [4].

1.1.4 Imaging studies

Imaging tests, such as a Computed Tomography (CT) or Magnetic Resonance Imaging (MRI) scans of the head, may be used to visualize the brain and surrounding structures. These can help identify any abnormalities or signs of inflammation.

Currently, guidelines recommend forgoing the lumbar puncture, while starting the treatment if there is clinical suspicion (regardless of whether the head CT scan is normal or not) of increased intracranial pressure or impending brain herniation [4].

1.2 Challenges in CSF WBC detection through the fontanelle of infants using conventional ultrasound imaging

White blood cells are a challenging target to identify within the CSF using high-frequency ultrasound due to their small size and location. The dimensions of the WBCs, are reported to fall typically between 9 and 18 μm [27]. Due to their small size, even at high ultrasound frequencies (20 to 75 MHz) cells are smaller than the wavelength of the incident sound wave (75 to 20 μm) . With sizes that can even go down to 5 μm, the intensity waves backscattered by this small cells are increasingly low. As an example, at a frequency of 50 MHz, the energy of the acoustic wave backscattered by a 7 μm diameter cell would be approximately 15 times less than than for the same type of cell but with twice the diameter [13]. Cells typically have acoustic properties similar to the surrounding tissue, leading to minimal acoustic impedance mismatch. This low contrast in acoustic properties makes it difficult to differentiate cells from background [13]. Additionally, ultrasound waves are attenuated as they travel through tissue, which can further reduce the signal strength. In general, not only because of their small size, but also due to their weakly scattering nature, the scattered sound of individual cells may be too low to be detected above background noise of the system [28], resulting in a relatively low Signal-to-Noise Ratio (SNR).

1.2.1 Depth attenuation

When ultrasound waves cross through the body before reaching the region of interest in the CSF, the intensity of the beam is attenuated. This attenuation depends on both the energy absorbed by the medium and the energy scattered by interfaces or tissue inhomogeneities. The fontanelle tissue constitutes the major hurdle affecting the quality of the ultrasound images on this application. Tissue may have different characteristics depending on the patient, which increases the variability of backscattered echo energy by cells

among different patients. For cells that are small compared to the working wavelength, energy is scattered in many directions, until being eventually absorbed due to particle vibration and heat production.

Attenuation at a given distance varies with ultrasound frequency. A high frequency wave is attenuated more than a low frequency. However, since higher frequencies allow more detail to be resolved, there is an inherent trade–off between resolution and penetration for different imaging applications. Resolution becomes essential when imaging small targets such as CSF white blood cells.

1.2.2 Resolution

Both spatial and temporal resolution must be taken into account. Spatial resolution is further divided into axial and lateral resolution. **Axial resolution** is the minimum distance where two reflectors located along the direction of the ultrasound beam can be distinguished. Axial resolution is dependent on the sound wave pulse length, referred as spatial pulse length (SPL). Specifically, axial resolution is equal to half the SPL. Spatial pulse length is the product of the number of cycles in an ultrasound pulse and the wavelength [29] .

$$\Delta_{axial} = \frac{SPL}{2} = \frac{\varepsilon\lambda}{2} \tag{1.1}$$

The number of cycles is caused by damping of the crystals after excitation. High damping reduces the number of cycles of the pulse and thus reduces the SPL. The pulse wavelength is given by the operating frequency of the transducer. High frequency transducers generate pulses of short wavelength [30].

Due to diffraction, the resolution of ultrasound imaging is theoretically limited to about half a wavelength. Below this limit, the echoes from many scatterers overlap and become no longer distinguishable. This leads to the fundamental trade-off between resolution and penetration depth, as attenuation increases with frequency. In general, conventional ultrasound imaging techniques cannot overcome the axial-resolution limit determined by the wavelength of the transmitted pulse.

Lateral resolution is the minimum distance at which two reflectors located perpendicularly to the direction of the ultrasound beam can be distinguished. Lateral resolution depends on the width of the beam and the frequency of the sound waves. A narrower beam width provides higher lateral resolution. The beam width can be reduced by focusing the sound waves as

they are produced by the transducer [31]. Beam focusing can be performed by using a piezoelectric focused transducer to produce an ultrasound pressure field, typically concentrated within a ellipsoid region. Lateral resolution is higher in the focal zone, where the beam width is narrower and can be assumed to be planar. Lateral resolution is also affected by the frequency of the sound wave, as higher frequencies tend to improve resolution [31].

Thus, the resonant frequency of the crystal, the design of the probe and, the rest of the system, are limited by this trade-off between resolution and penetration, restricting the requirements to a specific application.

Temporal resolution is the time elapsed from one frame to the next. It represents the ability to distinguish two events in time. Hence, it is essential for imaging rapidly moving structures. Time resolution becomes less crucial for the more static structures[32].

1.3 Methods to improve the resolution of ultrasound imaging

Improving the resolution of ultrasound imaging can be obtained by increasing the frequency, but there is a inherent compromise between penetration and resolution which limits spatial resolution by diffraction in far-field regime. Beyond increasing the frequency to improve the resolution, recent developments in optical microscopy have inspired analogous approaches to overcome the half-wavelength limit in ultrasonic imaging. Because of its relevance, we will review the different ultrasound-based approaches for super-resolution.

Ultrasound super-resolution imaging comprises several techniques, using high-frequency acoustic waves, that can distinguish objects or structures closer than the classical diffraction-limit. These techniques include ultrasound localization microscopy, super-resolution fluctuation imaging, structured illumination or near-field approaches [33].

Ultrasound Localization Microscopy, introduced in [34], and [35], is based on ultra-fast imaging for tracking the flow of contrast agents enabling to overcome the diffraction-limited resolution of vascular structures down to microscopic resolutions. This technique requires the injection of contrast agents into the body, in this case, gas microbubbles of a few micrometers in size . Because ultrasound is so sensitive to this pockets of gas, they can

be spatially separated to yield a precise positioning. Through a large number of acquired images, the subwavelength location of these many individual sources is accumulated to recreate a super-resolved composite image. These techniques are currently limited by low temporal resolution and long acquisition times [33].

Ultrafast imaging by using plane-wave emissions rather than line-by-line pulse echo, have increased frame rates to thousands of frames per second, enhancing blood flow sensitivity by more than an order of magnitude. This increase of sensitivity led eventually to ultrasound-based brain functional imaging, using the detection of small blood volume changes as a surrogate for brain activity [36]. Also inspired in optics, super-resolution fluctuation imaging exploits the high order statistics of temporal fluctuations in the ultrasound signal to reduce the size of the point-spread function of the images. An adaptation of this technique is proposed by [37], also using ultrafast tracking of contrast agents (microbubbles) to improve resolution. This method does not require the localization of individual emitters, therefore a smaller number of images are required. However, this process is limited to an improvement of resolution to a factor of 2 with respect to the resolution limit of the system. These techniques are now being applied pre-clinically and clinically for the imaging of the microvasculature of the brain, kidney, skin, tumors and lymph nodes [33]. Since contrast agents, such as microbubbles, typically remain within the vascular system, they generally do not cross the blood brain barrier (BBB). Therefore, they cannot reach or circulate in the cerebrospinal fluid or enter brain tissue, besides requiring an invasive procedure to inject the contrast agents into the body.

Another technique that increase the spatial resolution of ultrasound imaging is described by [38], inspired by structured illumination microscopy. The emission pattern is manipulated to encode the high spatial frequencies into the observed image through aliasing. Using post-processing techniques for the reconstruction of a super-resolved image, enhances resolution by a factor of 2 with respect to the resolution limit of the system. This method can be employed to improve vascular visualization.

The diffraction limit is applicable in the far-field regime. In the near field, the spatial resolution is proportional to the distance with respect to the object and independent of wavelength. Less than a few wavelengths away from a probe, according to [39] subwavelength sources can be differenciated at the 10- to 100-nanometer scale. However, if the target were organs in the

body, often at hundreds of wavelengths from the probe, and near-field super-resolution techniques are difficult to apply. In recent years, the introduction of metamaterials has enabled super-focusing in the near field achieving resolutions close to $\lambda/3$, which is beyond the diffraction limit [40]. According to [41], another way to overcome the inherent limits of spatial resolution is to combine ultrasound and other waves of different nature.

1.3.1 Methods to evaluate cell concentration in serous body fluids using ultrasound imaging

Studies have been previously proposed to characterize cell structure changes in cell ensembles using high-frequency ultrasound (20 and 40 MHz) [42]. From exploiting alterations in acoustic properties, such as spectral slope, variation in cell morphologies was detected. Due to problems with localization and low signal strength of cells, it is difficult to measure acoustic scattering from single cells, and thus, to achieve a comprehensive understanding of the scattering interaction at the cellular level. The first successful backscatter measurement from microspheres and individual cells was performed by [28] and compared with a proposed model of acoustic scattering from single cells. Using a refinement of this method to higher frequencies, [43] measured the backscatter response from two different cell types. A discussion of the characterization of colloidal mixtures by ultrasound, together with an account of scattering theory is presented in [44]. Studies of cell suspensions (with typical sizes in the range 6–30 μm at different concentrations) using ultrasound systems above 20 MHz have been conducted from the echoes backscattered by single cells [45], [46]. More recently, it has been shown by [14] and [15] that high frequency ultrasound (20-75 MHz) can be used to measure the ultrasound echoes backscattered by cells to detect low cerebrospinal fluid white blood cell concentration *in vitro*.

Despite all these advances, to the best of our knowledge, no practical solution based on ultrasound has been developed which can be employed for imaging directly the white blood cell concentration through the fontanelle of infants. Microscopic analysis of the CSF remains limited due, in part, to the lack of non-invasive imaging solutions providing microscopic resolutions.

1.4 About this thesis

The assessment of white blood cell concentration in the CSF is key to the diagnosis of meningitis. The proposed solution consist of a high frequency ultrasound based instrumentation capable of detecting backscatter signals from WBC in the CSF through the anterior fontanelle of neonates and young infants (See Figure 1.1). Considering the different anatomical characteristics of each patient, a mechanism is provided to locate a suitable view of the CSF. From this wide overview it is possible to zoom in (increasing lateral resolution) on a region of interest where the respective WBC concentration can be evaluated.

This solution builds on and extends the method proposed by [14] about an application of ultrasound imaging for *in vitro* assessment of WBC concentration from the measurement of the integrated backscatter coefficient of cells. This original proposal was based on a commercial platform that was adapted to the particular area of study.

In this context, this thesis focuses on the development of a complete portable ultrasound solution that can offer new possibilities for ultrasound research in this field by increasing the resolution to allow the counting of WBC in the CSF. This required the efficient integration of hardware and software components into a resource-constrained platform powered with AI capabilities to enable accurate CSF imaging and analysis according to WBC concentration. Furthermore, initial attempts have shown that this programmable platform can be adapted to fit specific requirements allowing rapid introduction and *in vivo* testing of new applications, such as peritoneal dialysis-related peritonitis and uveitis.

1.4.1 Motivation

The motivation for this thesis arises from the intention to allow a rapid access to detection of infant meningitis using non-invasive methods that accelerate screening, diagnosis and monitoring of this infection.

Lumbar punctures can be limited to only those patients whose screening is positive. Therefore, the number of negative tests can be reduced, eliminating the invasive procedure for the majority of suspected patients.

Although the initial focus of the application is on meningitis, its capabilities extend far beyond that. The application can enable the detection and monitoring of other infections in serous body fluids.

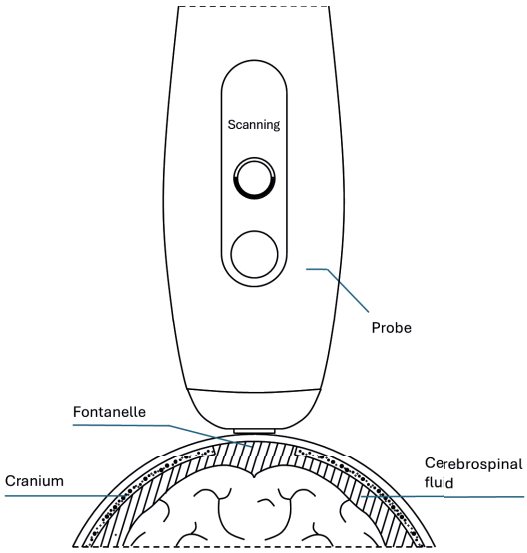


FIGURE 1.1: Cross-sectional cut of the proposed hand-held ultrasonic device to detect meningitis.

1.4.2 Hypothesis

It is possible to assess the concentration of white blood cells in the cerebrospinal fluid, below the fontanelle of a newborn, with a portable ultrasound device to confirm or exclude the suspicion of infant meningitis with minimal energetic impact on tissues.

1.4.3 Objective

The objective of this research is to design, implement and validate a portable ultrasound device to assess the concentration of white blood cells in the cerebrospinal fluid, below the fontanelle of a newborn, to confirm or exclude the suspicion of infant meningitis with minimal energetic impact on tissues.

The rest of this thesis is organized as follows. Chapter 2 continues with a review of the fundamental principles of ultrasound on which this thesis is based. Chapter 3 reveals the design of the hardware platform, defining the context for software development. Chapter 4 details the software implementation and system verification. Chapter 5 describes the optimization process and evaluates the results of the developed platform through *in vitro* and *in vivo* tests. Finally, Chapter 6 provides the main conclusions of the thesis and further directions of research.

Chapter 2

Fundamentals of ultrasound

The capture of high-quality ultrasound images depends critically on the physical interactions of sound with the tissues in the body. Understanding the physical principles of ultrasound is essential to find how images can be obtained optimally. Therefore, in Section 2.1, the physical characteristics of sound are introduced. The main methods used in ultrasound imaging are covered in Section 2.2, which have been selectively applied within the thesis. Section 2.3 is dedicated to the transducer, as it is essentially the primary working component of an ultrasound system. Section 2.4 discusses the propagation of sound waves through different tissues and how this affects image formation. Finally, despite ultrasound is generally considered a safe imaging modality, the potential bioeffects of ultrasound are explored in Section 2.5. Safety standards and guidelines are also discussed to ensure the responsible use of ultrasound in clinical settings.

2.1 Physical characteristics of sound

Sound is a mechanical wave that travels longitudinally in a medium. When a sound propagates through a medium, its molecules are alternately compressed and rarefied. Sound cannot be transmitted in a vacuum, it needs a medium for transmission, since the sound wave is a mechanical energy that is transmitted from one molecule to another. Notice that the molecules do not actually move when the sound wave passes through them, but oscillate back and forth, forming regions of compression and rarefaction in the medium. Therefore, the energy is transmitted through the medium without transfer of matter. Each repetition of this back and forth movement is called a cycle [47].

Frequency of a sound wave is the number of those cycles that occur per second, expressed in Hertz (Hz). Sound is classified according to the human ability to hear it. The range of human hearing is approximately 20 to 20000 Hz, termed audible sound. If the sound frequency is less than 20 Hz, below

TABLE 2.1: Frequency Spectrum of Sound

Sound Wave	**Frequency**
Ultrasound	Higher than 20 kHz
Audible Sound	20 Hz to 20 kHz
Infrasound	Less than 20 Hz

the limit of human hearing, it is referred as infrasonic or infrasound. If the sound frequency is higher than 20 kHz, above the limit of human hearing, is called ultrasonic or ultrasound (see Table 2.1). Operating frequencies in the range from 2 to 20 MHz and higher are commonly used in diagnostic ultrasound applications [47, 48]. Even higher frequencies (20 MHz - 100 MHz) are employed in special ocular, dermatological, and microimaging applications [49].

Frequency is dependent on the emitting source and is totally independent of the tissue that waves are interacting with [48]. Frequency affects penetration of sound and image quality. Frequency has a corresponding relation with resolution and an inverse relation with depth. The higher the frequency used, the lower the penetration, but the higher the image resolution [48].

The *wavelength* of a sound wave is the distance traveled during a complete cycle, usually expressed in millimeters (mm) in clinical settings. As shown in 2.1, the wavelength is denoted by the symbol lambda (λ), and can be calculated by:

$$\lambda = \frac{v}{f} \tag{2.1}$$

, where v is the velocity of the wave and f, its frequency. Thus, wavelength is influenced by both the sound source and the medium.

The speed of sound (propagation velocity) depends on the physical properties of tissue, especially determined by its density and elasticity (stiffness). As the tissue density increases, the propagation velocity decreases. On the contrary, the stiffer the tissue, the higher the propagation velocity. The propagation velocity can be considered approximately constant over the frequency range used in diagnostic applications. Therefore, the propagation speed of sound in soft tissue is typically considered 1540 m/s [50, 49, 48]. Table 2.2 shows the propagation speed of sound in air and in some biological media.

The resistance to the propagation of ultrasonic waves through tissues is defined as the *Acoustic Impedance*. Each type of tissue has a unique acoustic impedance. According to [49], acoustic impedance (Z) is the product of the density (ρ) and speed of sound in the tissue (v):

TABLE 2.2: Speed of sound in various media. Table extracted from [47]

Medium Type	Speed [m/s]
Air	330
Fat	1450
Water	1450
Soft Tissue	1540
Bone	3500

$$Z = v \cdot \rho \tag{2.2}$$

The strength of a sound wave can by quantified as acoustic power (P) or intensity (I). *Power* is the rate of energy transferred through the sound beam and is expressed in Watt (W). Power is proportional to the amplitude squared of a sound beam. *Intensity* is the energy concentration in a sound wave and is therefore the power delivered over a cross-sectional area of the sound wave. The intensity of a sound wave is calculated by dividing the power of a sound wave by its cross-sectional area, expressed in units of W/cm^2 [47]. The sound source determines the amplitude, power and intensity of the sound.

2.2 Techniques of ultrasound imaging

Diagnostic ultrasound is based on a pulse-echo principle in which short pulses of sound are transmitted into the body and the returning echoes are analyzed to create an ultrasound image (see Figure 2.1). The reflected echoes from tissue interfaces are caused by a mismatch in their acoustic impedance, which is the basis of ultrasound imaging. The interactions between ultrasound waves and the tissue during propagation will be detailed in Section 2.4.

In the traditional pulse-echo ultrasound method, signals are detected at a depth determined by the time delay between transmission and reception of the echoes. Time is converted to depth using the value of the speed of sound in tissue. This relationship may be derived from the equation 2.3:

$$d = v \cdot t \tag{2.3}$$

where, v is the speed of sound in tissue and t is the time taken from when the pulse is emitted until the return of the echo (round-trip travel time). The resulting value d must be divided by 2 to obtain the distance (or depth) of the reflector, to account for the trip to and from it:

$$d' = \frac{d}{2} \tag{2.4}$$

Once the echoes are received, they need to be processed to construct an image. This involves converting the raw echo data into a visual format. In the case of the display mode used in this thesis (B-mode), a point representing each returning echo is placed in a two-dimension (2D) image at the proper depth based on the time it took for the echo to return. Each point is also assigned a grayscale corresponding to the amplitude or intensity of the returning echo [49].

2.2.1 Ultrasound imaging modes

Several modes of ultrasound are used in medical imaging. This section covers the main formats that, in some way, have been used in this research.

A-mode (amplitude-mode) is the simplest format of ultrasound imaging. In A-mode imaging, a chart shows the returning ultrasound echoes with the horizontal axis representing depth in tissues and the vertical axis representing amplitude of the returning beam [51]. Originally, A-mode ultrasound was used in obstetrics in measuring biparietal diameters [47]. The A-scan still has a special use in ophthalmological examinations [49].

B-mode (brightness-mode) is the most commonly used format in ultrasound imaging. In B-mode imaging, 2D cross-sectional frames through the body are displayed in the traditional gray-scale format. The image is created depending on the intensity of the returning echoes, which determine the variation of shades of gray that form the ultrasound image [47]. If a sequence of scans is performed at a sufficiently high frequency, a continuous, real-time visualization of a given structure can be provided even when the structure

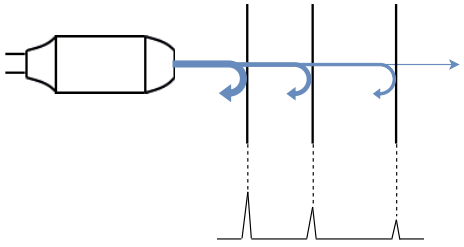


FIGURE 2.1: Traditional ultrasound techniques are based on the echo of the tissues due to the variation of their acoustic impedance. The echoes are very strong at first, and then decrease rapidly as the time-of-flight increases.

is in motion (real-time B-mode) [50]. Currently, three-dimension (3D) ultrasound images can be generated by acquiring consecutive B-mode ultrasound images at discrete step sizes along a predetermined path [32, 51].

M-mode (motion-mode) displays the echo data for a single scan line over time. This mode allows high temporal resolution, as only one scan line is acquired compared to the multiple lines acquired in B-mode to form an image. In M-mode, structures are represented in one anatomical dimension as each scan line represents new information over time. The M-mode data is displayed as a continuous function of time scrolling across the screen with depth on the vertical axis and time on the horizontal axis. This mode is mainly used to study fast moving structures such as heart-wall movement or valvular movement [32, 48].

Doppler mode imaging techniques utilize the Doppler shift principle in the detection and measurement of moving targets, usually blood. This mode is used for measuring vascular flow, velocity and frequency shift, among other applications [52]. Doppler imaging modes are out of the scope of this work, because they have not been shown to be useful for this particular application. Particularly, this mode is sensitive to the movement of red blood cells acting as scatterers. Nevertheless, a limited number of weak scatterers, which also move slowly, like WBC in the CSF, can be particularly difficult to distinguish, making Doppler ultrasound a deficient imaging technique for scenarios like this.

2.3 Transducers

Ultrasound waves are generated by transducers (also referred as scan head or probe [1]) packed with piezoelectric crystals. The crystal is commonly a disk-shaped element with a diameter of several millimeters and a typical thickness ranging from 0.2 mm to 2.0 mm [48]. When an electric current is applied to these crystals, they vibrates at the same frequency as the excitation and produce an ultrasound wave. The ultrasound wave passes through the body at the same frequency generated. Conversely, when the ultrasound wave returns to the transducer, the crystals change in shape, generating a small electric current. Thus, these crystals in the transducer transform electric energy into mechanical energy (ultrasound) and viceversa. Transducers

[1] In this work, this term will not be used to refer to the transducer, to avoid conflict with the hand-held probe built specifically for this application, and referenced in the later sections.

commonly have crystals made of lead zirconate titanate [47], because of its high conversion efficiency.

The application of these transducers varies according to the working frequency range. The frequency of a given transducer depends on the thickness of the crystal. The transducer bandwidth is the frequency range in which the crystal operates [48]. Most modern transducers are capable of multi-frequency operation, which is called broad bandwidth. A range of frequencies is produced, consisting of a preferred (central) frequency in addition to higher and lower frequencies [49].

Generally, a single crystal is not sufficient to generate an ultrasound wave for clinical imaging. Modern transducers may have a large number of crystals arranged into a line, a phase, a matrix, or an annular array, depending on the application. The configuration of the transducer structure determines the area and shape of the image produced.

2.3.1 Coupling interface

There is a major acoustic impedance mismatch between the transducer elements and the body. The acoustic impedance mismatch requires matching layers to transmit energy efficiently. The crystals are protected by a coating that reduces the resistance to sound propagation (impedance) from the crystals to the body. The ultrasound produced by a transducer do not travel effectively through air. Transducers, therefore, must be directly coupled to the patient's skin without an air gap [53]. In order to enhance the energy transfer from the transducer to the patient's skin, an aqueous gel is added that couples the transducer to the skin and allows the sound to come and go.

2.4 Propagation in Tissues

When an ultrasound wave traveling in an acoustically uniform medium reaches an interface with a medium of different characteristic mechanical impedance (Table 2.2), the waves are partly absorbed, but reflection and refraction also occurs.

2.4.1 Reflection and refraction

For the case of an incident wave on a theoretically plane surface of a tissue (larger than the ultrasound wavelength), the echo is reflected back from the

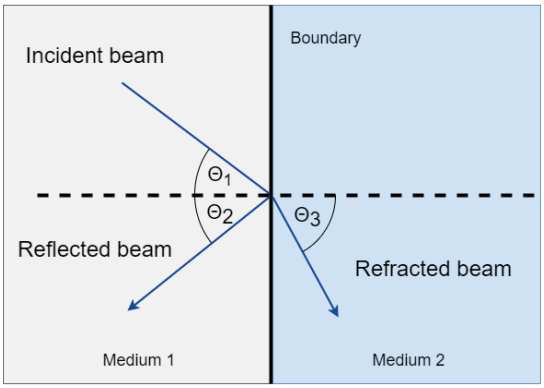


FIGURE 2.2: Reflection and refraction of ultrasound beams.

boundary at an angle equal to the angle of incidence (specular reflection), as shown in Figure 2.2. The transmitted beam deviates from its straight line (refraction) by an angle that is dependent on the difference in ultrasound velocities on both sides of the boundary [53].

The amount of reflection depends on the angle of incidence of the beam and the difference in the acoustic impedance of the two surfaces. The angle at which ultrasound waves reach a structure is called the angle of incidence. Ideally, structures are expected to be imaged with an angle of incidence perpendicular to the surface (normal incidence), because reflected waves return to the transducer in the greatest intensity (optimal reflection). When waves interact with a structure at an oblique angle, fewer waves echo back to the transducer, decreasing both the brightness of the structure and the resolution [48, 54].

The amplitude of the returning echo is proportional to the difference in acoustic impedance between two tissues when the sound wave passes through their interface [49]. If two tissues have the same acoustic impedance, their boundary will not produce any echo. If the difference in acoustic impedance is small, a weak echo will be produced and most of the ultrasound will pass through the second medium. If the acoustic impedance difference is large though, a strong echo will be produced [53]. Typically in soft tissues, the amplitude of the returning echo at a boundary is only a small fraction of the incident wave amplitude (known as hypoechoic or anechoic). Areas containing bones or air may produce echoes so large that insufficient ultrasound left to image beyond the tissue interface (known as hyperechoic). This large reflection decreases the penetration of sound waves into deeper tissues and can cause artifacts in the image [31]. This is the reason why the operator must avoid these areas and use specific windows in order to image deeper structures effectively. Strong returning echos appear on the ultrasound image as

white and weaker reflections as shades of gray [53].

Ultrasound imaging is entirely dependent on the returning echoes. On the other hand, refraction is a source of ultrasound artifacts. Since all ultrasound scanners operate under the assumption of an ideal situation, in which waves always travel in a straight line, it will not be known if any pulse has been deviated from its trajectory [48]. In general, ultrasound energy will be lost at the receiver transducer if it is reflected or refracted away from the returning line of sight or if the beam is deflected.

2.4.2 Absorption

The acoustic absorption is caused by the conversion of the ultrasound energy into heat. This is mainly due to friction forces of the molecules in the transmission medium while vibrating in response to the propagation of a sound wave. Absorption is very low in fluid media, intermediate in soft tissues, and very high in bones and gases at the frequencies used in diagnostics [50]. When assessing the biological effects and safety of ultrasound, the production of heat in tissue is an important factor [49].

2.4.3 Scattering

Various tissue interfaces reflect differently, impacting the overall image quality. Smooth interfaces are treated as specular reflectors and reflect a high proportion of waves to the receiving transducer. Specular reflectors differ with irregular interfaces (shorter than the incident wavelength) called scatterers or diffuse reflectors, which cause the sound waves to be deviated away from the transducer, affecting the image quality. Weak returned echoes can only be visualized when they are abundant and tend to reinforce each other, producing ultrasound *speckle*. Red blood cells cause this type of scattering, so the waves are scattered in all directions [48].

2.4.4 Attenuation

Attenuation describes the loss of acoustic energy as the sound waves travel through tissues. Propagating energy can be attenuated to the receiving transducer when ultrasound signal is attenuated product of reflection, refraction, absorption or scattering.

In short, reflection and refraction occur on surfaces that are large compared to the ultrasound wavelength. For objects that are small compared to

the wavelength, the energy is scattered in many directions, to end up being absorbed as particle vibration and heat production. As mentioned in Section 1.2, attenuation varies as a function of ultrasound frequency, with the respective trade-off between penetration and resolution. As the change in intensity due to attenuation can be very large, the relative change in intensity is measured in decibels (dB). The attenuation is equal to approximately 0.5 dB/cm/MHz in soft tissues over the round-trip distance [49, 54].

2.5 Bioeffects of ultrasound

Ultrasound is generally considered a safe imaging technique, because it is a non-ionizing form of energy that is applied non-invasively, compared to other imaging modalities that involve ionizing radiation such as X-rays and CT. However, ultrasound introduces energy into the body. Diagnostic levels of ultrasound can cause physical effects on tissues, such as pressure oscillations with consequent mechanical effects and increased temperature [55]. Therefore, the applied sound intensity must be limited to meet the safety standards of diagnostic ultrasound.

Regulatory bodies define specific limits to prevent potential harm to the patient. The United States FDA regulates the maximum power of ultrasound systems for patient safety. The permitted acoustic output depends in part on the type of application [49]. The primary metrics to regulate the acoustic output are the TI and the MI, which are mandatory in modern ultrasound devices.

The TI provides a relative indication of thermal risk during diagnostic ultrasound explorations [56]. It is defined as the ratio of the acoustic power at the depth of interest to the estimated power required to produce a temperature rise of 1 in the tissue examined [57, 58]. The MI is a measure of ultrasound beam power, which indicates possible non-thermal bioeffects of the acoustic field, such as cavitation and streaming [59]. Is is defined as the maximum negative pressure divided by the square root of the ultrasonic wave frequency [60].

The TI and the MI are not perfect markers of thermal and non-thermal bioeffects risks, but are recognized as the most practical and easily understood methods of assessing the potential of these risks [47]. Despite the lack of scientific evidence confirming the harmful bioeffects of exposure to diagnostic ultrasound, the as low as reasonably achievable (ALARA) principle should be applied when adjusting the controls of the ultrasound system in

order to reduce any risk. According to the FDA, it is recommended that the MI should not exceed 1.9 for diagnostic ultrasound procedures. On the other hand, it is generally advised to keep the TI as low as possible, typically below 0.7.

Chapter 3

System design

This chapter delves into the fundamental aspects necessary to develop the application. First, the system requirements are delineated in Section 3.1 to establish a clear understanding of the functional and performance expectations that guide the work. Following this, the critical design choices influencing the system performance and robustness are discussed in Section 3.2. This includes discussions on component selection, design trade-offs, and considerations that have influenced the overall architecture of the system. An overview of the system architecture is provided in Section 3.3, showing the critical interaction between hardware components and software modules. Then, the proposed design methodology is described in Section 3.4, highlighting the iterative and incremental approach that ensure continuous integration into the solution, as well as verification and optimization of the results. In addition, the tools and technologies employed in the development process are presented.

3.1 System requirements

Some features should be taken into account before defining an ultrasound imaging methodology for the evaluation of WBC concentration in the CSF. Diagnostic ultrasound scanners are built from several essential components. A pulser excites the piezoelectric crystals inside the transducer, transmitting pulses of ultrasound into the body. Returning echoes to the transducer are acquired and conditioned by the receiver and then processed by a CPU to reconstruct and analyze anatomical images that are shown on a monitor.

3.1.1 Transducer

The transducer essentially acts as the primary working component of an ultrasound system. A wide number of different transducers are available

for every commercial ultrasound equipment. Transducers are usually carried in a hand-held probe, but they can be placed on the tip of a catheter for intravascular examinations or on a stationary arm for Ultrasound Biomicroscopy (UBM) [31]. When selecting the working frequency range of the transducer, the inherent trade-off between resolution and penetration depth must be taken into account. In some imaging applications, more than one transducer may be necessary to take advantage of the particular configurations, as described in section 2.3. Understanding the capabilities and limitation of the transducer is essential to obtaining high-quality images.

3.1.2 Probe cable - Preamplifier

For connecting the transducer to the rest of the system, a relatively long cable (about 2 m) is usually required. If a transducer array is used, this cable may have a considerable number of micro-coaxial cables, making it a very expensive part of the system. In addition, they could become very stiff and unwieldy because of the many cables to manage the multiple elements in the transducer.

In many systems, the transducer elements are connected directly to the probe cable, which can result in substantial signal losses due to the capacitance loading of the cable on the transducer elements. Depending on the transducer and operating frequency, a loss in the order of 1 to 3 dB can be anticipated [61]. Misalignment and cable losses directly increase the Noise Figure (NF) of the system. This means that the first amplifier after the cable must have a NF that compensates the degradation caused by the cable. One way to work around this issue is to install an amplifier in the probe.

3.1.3 Pulser - Receiver

A pulser generates precisely timed high-voltage pulses to the crystals of the transducer, which emits short bursts of ultrasound waves into the body. The image is created from the echoes that return to the transducer from the tissues after each pulse. Pulser parameters can be adjusted to configure the pulses that excite the transducer. This configuration affects the acoustic energy that is transmitted into the body. Specifically, this pulses should have sufficient amplitude to effectively compensate for tissue losses with an adequate SNR. However, the amplitude should be limited to meet safety standards during clinical examinations.

On the other side, when the echoes return to the piezoelectric crystals inside the transducer, a small electric current is produced towards the receiver. The sampling rate of the receiver should be high enough to prevent aliasing, according to the *Nyquist* theorem. Due to attenuation, the dynamic range of the received signal can be quite big over the depth of penetration, even after amplification. Therefore, the digitalization of incoming analog signals should be performed at a high bit resolution to achieve the maximum image quality. To create the best possible image, these weak electric signals must be manipulated by adjusting various receiver parameters. In addition, digital signal-processing methods can be applied to enhance the information content of the received signal.

In general, ultrasound examinations are highly interactive and operator dependent. Thus, great flexibility is often required to system reconfiguration of data acquisition sequences and parameters. This is an important aspect to consider for researchers who are interested in investigating new imaging applications.

3.1.4 Main computing platform

All ultrasound systems have a CPU to create the anatomical images. However, high computing capabilities are essential for high resolution ultrasound imaging and processing at the high acquisition rates. Furthermore, the deployment of DL models for WBC concentration estimation will certainly increase the hardware requirements for AI inference. Such specialised hardware requires specific processing components and development frameworks to enable the deployment of AI models developed on high-performance computing (HPC) platforms. As a goal, our portable medical device must implement on-board all analog signal and digital image processing tasks without requiring any external computer or connection. This requires using multiple heterogeneous computing platforms and a strategy to assign the required tasks to them. The embedded application running such a multiprocessor system must be easily upgradable by installing software without having to change the hardware platform.

3.1.5 Functional requirements

The whole instrument, especially the probe containing the ultrasound transducer, is designed according to the specific characteristics of the application, which demands high spatial resolution to be able to visualise the WBC within

the CSF. As the pooled mean size of anterior fontanelle of a infant is around 2.58 cm [62], there is a physical limitation to the size of this acoustic window that allows the access to the CSF, while avoiding the skull bone. By laterally scanning the CSF with a mechanically-driven transducer, a high lateral resolution can be achieved, which is functionally dependent on the size of the steps to be followed within a given path. Each frame will be created from a sequence of acquisitions, each of which generates one scan line. Ultrasound image formation is highly sensitive to alignment and mechanical control, as well as synchronization between the scanning motion of the transducer and the data acquisition process. Several challenges have to be overcome for the implementation of the probe, including those related to its configuration, such as mechanical stability, micro-positioning, regulation of the distance to the target, and signal handling and detection.

The whole chain related to the generation and analysis of a high-resolution ultrasound image requires the concurrent execution of several functionalities. These tasks include: probe control, ultrasound signal acquisition, parameter configuration, digital signal processing, image composition, user interface and overall system management to finally provide an estimation of the WBC concentration in the CSF. The real-time operation of this solution is essential for immediate diagnostic feedback, enhanced image quality, patient safety, and operational efficiency. It allows clinicians to make timely decisions, guide interventional procedures accurately, and continuously monitor physiological changes. Real-time imaging reduces scan times, improves patient comfort, and streamlines workflows, leading to higher diagnostic accuracy and better patient outcomes.

3.2 Related design choices

3.2.1 Transducer

The choice of transducer frequency is an essential consideration to ideal ultrasound image acquisition. Since axial and lateral resolution is improved as frequency increases, higher frequency transducers are usually selected for resolving small objects in the ultrasound image. As mentioned in previous section, one limitation of using high frequencies is that, as the frequency increases, the penetration of the sound wave decreases. By recognizing this intrinsic compromise, the user can choose the highest frequency transducer that penetrates to the depth of the target structure. For example, a 5-MHz

TABLE 3.1: Characteristics of the selected transducer

Central frequency	20 MHz
-6 dB bandwidth	10 - 30 MHz
Element diameter	10 mm
Focal distance	18 mm

transducer should be selected to analyze depths in the range of 12 to 15 cm [31]. A 15-20-MHz transducer may image depths of only 3 to 4 cm. Higher frequencies like 30-40 MHz may penetrate only 1 to 2 cm [32].

Specifically, an increasing backscattering amplitude was found by [43] as the frequency rose up to 30 MHz for human acute myeloid leukemia cells (11.5 μm diameter). Also considering the downward shift in the center frequency of ultrasound pulses that propagate through biological tissues, as a result of the attenuation dependence on the frequency, [15] concluded that the optimum operating frequency could be below 30 MHz for similarly sized cells.

A single-element transducer that operates at 20 MHz with a bandwidth (-6dB) ranging from 10 MHz to 30 MHz has been employed considering the restrictions of the application. This frequency compensates for the loss of cellular backscatter energy with lower attenuations of the ultrasound beam as it travels through tissue [15]. This is a custom focused transducer with an aperture of 10 mm and with the focal position (optimal spatial resolution) placed at a distance of 18 mm (focal distance) from the transducer emitting face, according to the region of interest. A focused transducer was selected to enhance the amount of energy reflected from the cells. The characteristics of the employed transducer are shown in Table 3.1 The pulse echo response of the employed transducer is shown in Figure 5.2.

When the crystal is excited, about two or three wavelengths are transmitted in each pulse before a backing block inside the transducer dampens the vibrations. Thus, the SPL is approximately two or three wavelengths. The SPL, which depends on the transducer frequency, determines the capability to separate points along the sound beam axis (axial resolution). Axial resolution cannot be higher than half the spatial pulse length due to overlapping of reflected echoes from closely spaced interfaces [49].

As mentioned above, the temporal resolution is not as critical when imaging target structures are relatively static, such as the CSF. However, a high acquisition rate of scan lines is essential to ensure lateral coherence within the image.

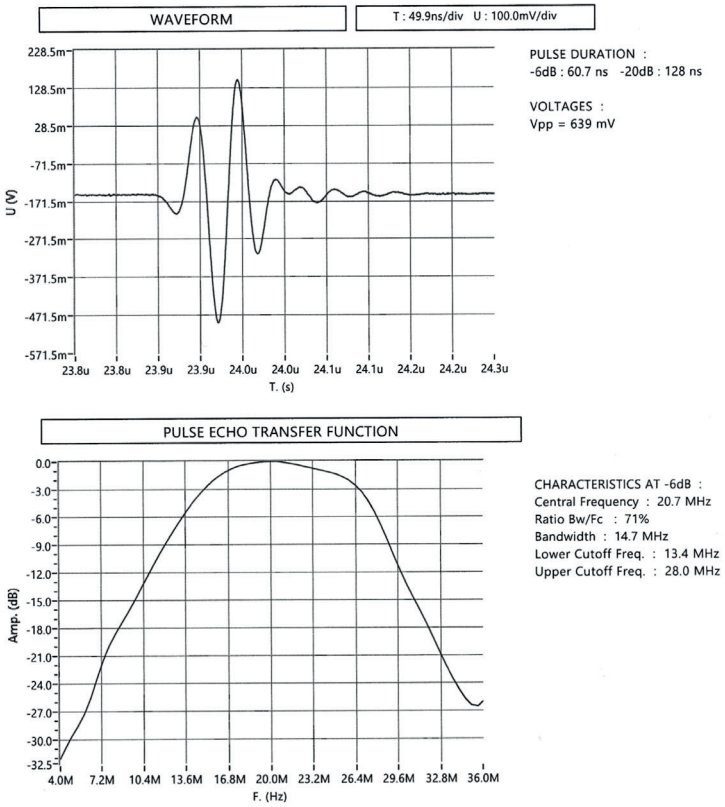


FIGURE 3.1: Pulse–echo impulse response and spectrum of the selected 20-MHz transducer.

3.2.2 Probe cable - Preamplifier

Some cost-effective design criteria have been established to reduce the thickness of the cable and facilitate proper handling of the probe. Using a single transducer element reduces the number of micro-coaxial cables to just one while cutting most wiring cost. Transceiver modules were designed between the probe and the main base board to transparently move serial data over DC power supply lines. The communication signal is OOK modulated /demodulated on the power line. OOK is a simple and common form of Amplitude-Shift Keying (ASK) modulation that represents digital data as the presence or absence of a carrier wave. This way, UART cables are replaced by the ubiquitous power line to turn it into a half duplex communication system. This helps to achieve the portability requirements through a lightweight cable that is easy to handle by the operator.

The preamplifier (32 dB) was no placed inside the probe due to mechanical design constrains related to space limitation, as it would require an unaffordable implementation cost. It has been included in the main base board of

the device and the transducer is wired through the probe cable to the preamplifier.

3.2.3 Pulser - Receiver

For this particular application, Difrascope pulser-receiver from Dasel Sistemas[63] was selected. It is a portable multi-channel system with excellent performance and powerful signal processing capabilities. Its configuration parameters can be set independently for each transmission and reception channel. Pulses are transmitted as square-waves and can operate in burst mode. In the receiver path, an attenuator and a voltage-gain controlled amplifier provide differential signals up to the Analog-to-Digital Converter (ADC). The analog stage uses an anti-alias filter that limits the signal bandwidth to 30 MHz (-3 dB). High sampling performance of the received signal is provided with 14-bit resolution ADC and sampling rates up to 100 MHz. Data samples from the ADC are received by an Field-Programmable Gate Array (FPGA), which comprises a pipelined architecture with multiple Digital Signal Processing (DSP) functions together with other control functions, like parameter configuration. As all the processing functions are performed in parallel, results are available in real-time. The processing chain includes averaging echoes over several cycles, programmable FIR filtering and accurate envelope extraction, among other functions. The DifraScope unit provide interfaces to encoders and external triggers to synchronise the acquisitions. Ethernet communication can be established with a host computer to configure the ultrasound system and transfer data for further processing, display and storage.

3.2.4 Main computing platform

The NVIDIA Jetson Nano [64] is ideal for this application, providing powerful computing capabilities suitable for AI tasks, such as image classification. Despite its high performance, the Jetson Nano is designed to be energy-efficient, making it suitable for applications where power consumption is a concern, such as portable or battery-operated devices. The small size of this module allows for easy integration into embedded systems or devices with limited space, making it ideal for applications where size constraints are important. With its integrated NVIDIA GPU, the Jetson Nano offers

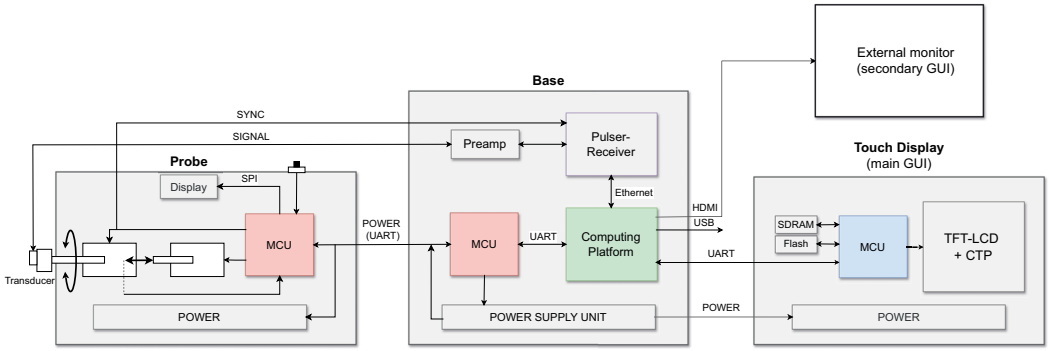


FIGURE 3.2: Block diagram of the system

hardware acceleration for AI algorithms, enabling faster processing and real-time performance for computationally intensive tasks. This platform is well-supported by NVIDIA software development tools and libraries, making it easier for developers to prototype, deploy, and optimize their applications. Overall, the NVIDIA Jetson Nano is a versatile and cost-effective solution for a wide range of AI applications, offering high performance, low power consumption, and developer-friendly features.

3.3 System architecture

The proposed architecture is based on a heterogeneous computing platform, consisting of different modules connected to execute the different tasks of the system. Each subsystem is based on a commercially available processing units selected to maximize the speed-energy-cost trade-off. Figure 3.2 shows a block diagram of the system with colored processing units.

NVIDIA Jetson Nano: this embedded computing board acts as the main computational element of the platform, controlling and coordinating the different tasks implemented in each subsystem. Its main application software controls the functions of the ultrasound system: data acquisition, parameter configuration, digital signal processing, image composition as well as user interface, storage, plotting and data visualization. The Jetson Nano is the computational core of the system, facilitating data exchange and communication between the different components. This application provides an secondary user interface (the Touch Display is the main GUI) for system configuration, monitoring, and extended interaction. Tools for analyzing and obtaining quantitative measurements from the ultrasound signal are also available. AI capabilities are integrated to provide automatic and accurate classification of patients according to their WBC level in the CSF.

Probe: this module, based on PIC32MK_GP Microcontroller Unit (MCU) from Microchip, controls all the probe peripherals according to the instructions received from the Jetson Nano. A button on the probe starts the scanning process. The mechanical motion of the structure that holds the transducer is controlled by two stepper motors allowing to position (in depth) and move the transducer during acquisition. A photo-detector sets the safe limits and identifies reference positions within the direction of penetration of the transducer. Complementary user information is shown on a local small display.

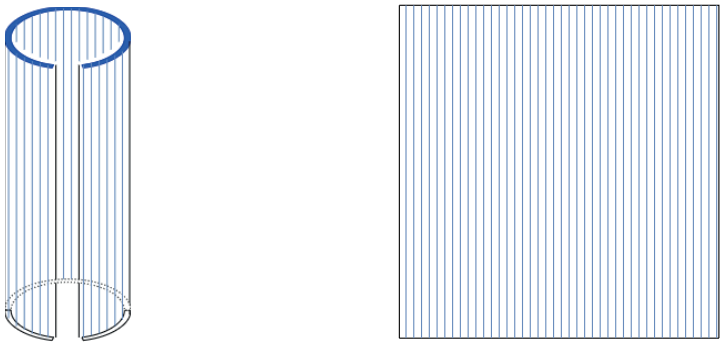
Base MCU: a similar PIC32MK_GP MCU acts as communication bridge between the Jetson Nano and the probe. Also, it controls the operation of power devices, system power-on and power-off sequences, monitors power requirements and protects against faults. This module ensures efficient and reliable power management within the system.

Touch display: this is the ETEMB050013XDHAL embedded GUI module from EDT [65]. It is based on the STM32F750 MCU from STMicroelectronics and manage the main user interface of the system. This block facilitates a seamless and responsive user experience by connecting the GUI with the underlying application logic. It includes the integration of touch functionality into the overall application, as well as a mean to present the information.

3.3.1 Operational basis

The ultrasound images are generated by the acquisition of consecutive scan lines (A-scan) at discrete step sizes moving along a pre-determined path to build B-scan images. This path is the result of the mechanical motion of the single transducer around a fixed rotation axis, to prevent a one axis path being longer than the size of the fontanel. As shown in probe module in Figure 3.2, a motor rotates a holder containing the transducer element, placed 2 mm away from its central axis. This arrangement allows the transducer to traverse an arc-shaped path (highlighted as a dark blue arc in Figure 3.3a) of 331.2 degrees , describing 11.56 mm back and forth displacements in a plane perpendicular to the direction it is pointing to.

On each motor step, one scan line is formed (highlighted as light blue vertical lines in Figure 3.3a) by sending a pulse from the transducer and then, the reflected signals from different depths are recorded. Sequential scanlines are acquired across the body and composed together into a high spatial resolution 2D B-mode image. As the transducer element is moved on the



(A) (B)

FIGURE 3.3: (a) Surface sensed during image generation; (b) Acquired image as shown on display.

same plane during acquisition, the unrolled image has a rectangular shape, as shown in Figure 3.3b. This way, the caputred ultrasound images are displayed on the monitor.

This method has the related drawback of an increased acquisition time or storage requirements. However, the temporal resolution is not so critical when imaging target structures that are relatively static, such as the CSF. On the contrary, a high acquisition rate of scan lines is essential to ensure lateral coherence within the image.

As shown in Probe module in Figure 3.2, by means of another motor the structure that holds the transducer element can be moved along the direction the probe is pointing to. This allows to slightly penetrate (the acquisition window) and subsequently image deep into the body without increasing the acquisition delay with the consequent depth attenuation. In this way, the area of interest can be aligned with the focal zone for the optimal range of transducer resolution.

3.4 Methodology and tools

When developing software for any embedded system, it is essential to follow certain guidelines and take into account many different factors so that its implementation can work properly and can be completed on time. As designs become more complex, the need to follow an ordered method to achieve good results becomes more important. In general, the design flow is a cycle and includes several intermediate steps. In many cases the process is non-linear. If failures or problems are discovered in the system, the previous steps must be iterated over again to correct them.

In this case, the workflow started with a review of the fundamental principles of ultrasound, as they are the basis for all the design solutions implemented. This study was essential for the various phases of system optimisation. Then, a set of requirements were defined for the implementation of the system. These specifications are given by the criteria that this application must follow to meet the expected results.

After that, another working group built the hardware platform, including the whole set of physical components required to perform the very specific functionalities according to the application requirements. At the same time, this design is flexible enough to be able to adapt to new requirements of other applications on serous body fluids.

The key part of this thesis consisted on the software implementation of the system. Each software unit was developed separately for each module that integrates the system. Over several iterations, each module was verified to ensure that the software meets the expected requirements. During this process, the hardware platform was fine-tuned and new software solutions were proposed. When each module was working correctly, it was integrated into the system. Test at system level were also performed following the same systematic approach.

Finally, the assessment of the system performance was conducted according to its different configurations. At the same time, the quality of the measurements was optimised while taking into account the trade-off with the safety limits. Incorrect or unexpected results led back to refinement of the solution. Figure 3.4 shows the workflow used in the development of the system.

3.4.1 Tools

Probe / Base

The same tools were used to develop the control firmware for the probe and the base MCU, as both modules are based on Microchip's PIC32 microcontrollers. MPLAB X Integrated Development Environment (IDE) was employed for comprehensive development and debugging with the support of MPLAB XC32 Compiler optimized C/C++ code. MPLAB Harmony framework simplified the peripheral configuration and code generation. The MPLAB ICD 4 was the tool of choice for programming/debugging the hardware.

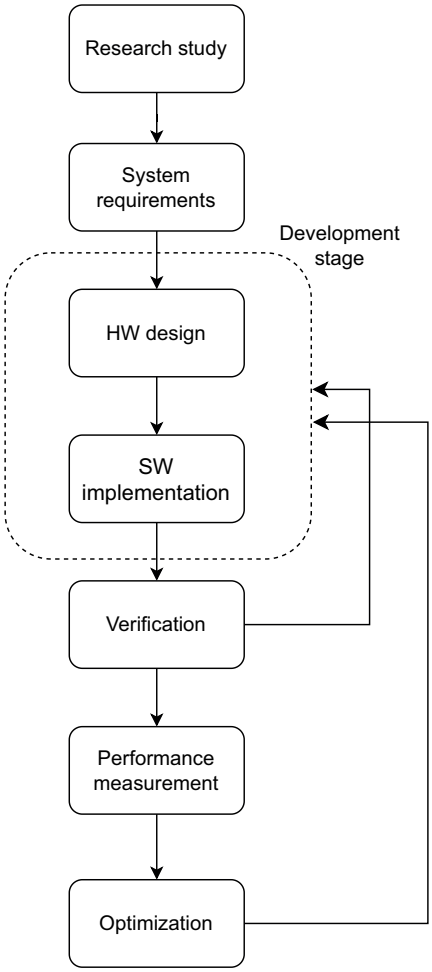


FIGURE 3.4: System design flow

Jetson Nano

The Jetson Nano primarily runs the NVIDIA JetPack Software Development Kit (SDK), which is a comprehensive software stack tailored for the Jetson platform. JetPack includes a Linux-based operating system called Linux for Tegra (L4T), which is based on Ubuntu. Specifically, JetPack integrates a wide range of AI and system software, tools and libraries, like CUDA or cuDNN, designed to provide end-to-end development workflow for accelerating AI applications. In addition, JetPack provides support for TensorRT [66], a framework for model deployment optimized for NVIDIA specialised GPU hardware. This way, developers can access directly to GPU accelerators through a common high-level C++ Application Programming Interface (API) (also a Python API is available) for high-performance deep learning inference. C++ API is the tool of choice for real-time applications where performance, as well as security, is critical. All these features provides a robust environment for developing and deploying AI-powered applications on the Jetson Nano. In this context, Qt has been integrated with JetPack SDK to exploit a unified framework from Qt Creator and build a GUI application software in C++ that leverage all the technologies in this embedded platform.

Touch Display

For developing the main GUI using a resource-limited STM32 MCU, TouchGFX enabled the creation and visual customisation of the graphical part of the application. On the other side, the firmware was written, compiled and debugged using STM32CubeIDE. The tool selected for programming and debugging the hardware was the ST-LINK/V2.

Chapter 4

Software implementation and verification

This chapter describes the software implementation of this advanced ultrasound scanner. Several components were efficiently integrated into a single solution to enable accurate imaging and data analysis. First, Section 4.1 explores the software mechanisms that drive the operation of the probe to ensure high-quality image acquisition through precise control of the transducer element. Section 4.2 examines the software infrastructure that supports seamless communication and integration between the various components of the system. The implementation details for (i) the power control stage of the whole system from the base MCU, as well as (ii) the main GUI on the touch display are not covered in the thesis, to avoid diverting attention from more singular development issues of this application. Subsequently, Section 4.3 covers the entire data management process within the system, including accurate acquisition of ultrasound data, configuration parameters, and digital signal processing to obtain clinically relevant information. Finally, the integration of artificial intelligence capabilities into the application is described in Section 4.4, focusing on the deployment of a neural network (NN) model for the evaluation of white blood cell concentration.

4.1 Probe control

As already introduced in section 3.3, the probe incorporates a housing that holds the transducer, which can be mechanically moved in two different planes by each of the associated stepper motors. As scan lines are acquired while moving the transducer, precision motion control is required to ensure ultrasound images are created with lateral coherence. Each of the two stepper motors requires a STSPIN820 driver, as shown in Figure 4.1.

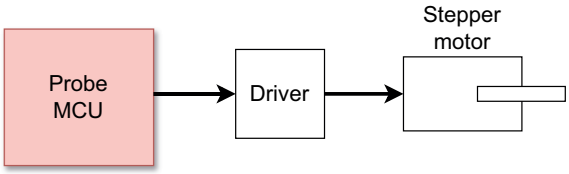


FIGURE 4.1: Block diagram of each stepper motor control.

Control firmware on the MCU must manage the driver of each stepper motor to move the transducer with a controlled and precise angle. The STSPIN820 drives the motor step by step according to the step clock. A square wave is generated by the MCU using an Output Compare module that toggles its output responding to the selected time base events from a timer. This pulse train is applied to the step clock input pin of the driver to trigger discrete movements at equally spaced intervals (steps) defined by the period of the wave. MCU enables the driver, sets rotation direction and the microstepping mode through its digital output ports. The current consumption of the stepper motors is independent of its load (unlike DC motors). Therefore, when they are enabled, they consume more current even if they are not working. This is why they are disabled during scanning between one rotation and the next, to prevent them from getting too hot and to save energy. After each rotation, the direction is inverted to ensure the intended back and forth displacements. Increasing the microstepping resolution of the scan motor results in a smaller angle between the steps, which results in a smoother movement of the transducer.

The majority of these stepper motors do not have integral position feedback. Although high precision can be obtained by running in open loop, limit switches or home detectors are typically required for safety and/or to establish a reference position. In the probe, the range of the scan motor is mechanically limited by a metal stop that prevents the motor from twisting the transducer cable around the motor axis. For the depth motor, a photodetector detects the home position. The photodetector has been connected to a digital input interface in the MCU, configured as comparator. The photodetector output signal is compared to a precise reference voltage generated by an internal Digital-to-Analog Converter (DAC). Whenever the photodetector detects a metal plate indicating the maximum depth the transducer can reach, an MCU interrupt is triggered.

A push-button on the probe starts the scanning process. This button is monitored from the corresponding MCU input pin, configured to generate an interrupt request when a change in the pin state is detected.

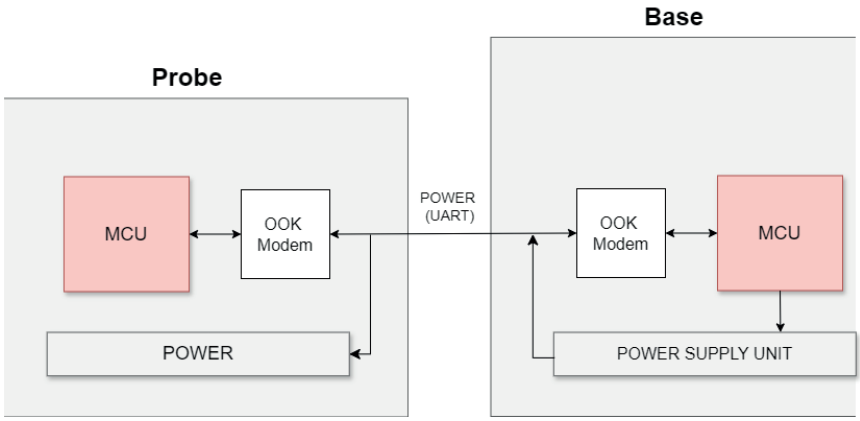


FIGURE 4.2: Block diagram of the probe-base UART communication using OOK modulation over the DC power line.

A small Liquid-Crystal Display (LCD) display in the probe guides the user during the operation with auxiliary information. From the MCU side, another Output Compare module has been configured (together with its corresponding timer) in Pulse-Width Modulation (PWM) mode to generate a pulsing signal to power the back light of the display. The brightness of the probe display changes proportionally to the PWM duty cycle. A 4-wire master mode SPI interface on the MCU has been configured with a baud rate of 10 MHz to control the display, according to its communication protocol.

4.2 Inter-module connectivity

4.2.1 Probe - Base

Section 3.2.2 already introduced the solution selected for data transfer between the probe and the base: the OOK modulation of the UART communication signal over DC power signal. At the same time, power supply is continuously provided to the probe (see Figure 4.2). Each MCU module, probe and base, must manage this modulation scheme to ensure effective communication.

UART communication has been configured with the same settings on both sides, which is mandatory for proper operation. The most common setting of 8 data bits, no parity and 1 stop bit (8N1) has been used at a baud rate of 9600 bps. Hardware flow control option is disabled. Data exchange has been configured in non-blocking mode to trigger an interruption each time a data reception is completed.

OOK modulation / demodulation of the UART communication signals uses a carrier to encode the transmitted bits. The carrier is generated from the transmitting side, so that only one side can transmit at a time, turn it into a half duplex communication system. The MCU in the probe and in the base can send and receive data with each other, but not simultaneously. Communication is unidirectional at a time while providing power to the probe. The carrier frequency needs to be greater than the communication baud rate. Specifically, a 1.18 MHz carrier is generated from each side, using another Output Compare module configured in each MCU to toggle its output according to the events generated from its respective timer. This way, the UART communication signal drives the output-enable input of a single buffer such that, when the input value is 1, the carrier signal is transmitted, but when the input value is 0, the carrier signal is not transmitted. In other words, the presence of a carrier wave represents a binary 1, while its absence represents a binary 0.

On the other side, when this transmitted signal reaches the receiver, a demodulator decodes data, according to the encoding scheme used by the modulator. The amplitude of the received signal determines the bit it represents, thus recovering the original data. Specifically, the received signal is fed to a comparator configured in the system MCU at each end, in this case, at the one currently acting as the receiver. This input is compared against the supply voltage. The comparator output is enabled (and inverted) to appear on an output port of the MCU, which in turn is connected to the configured UART reception port. A received signal amplitude above a decision threshold (i.e. presence of carrier) corresponds to a transmitted binary 1 and a binary 0 is set when the received signal amplitude is below the decision threshold (i.e. absence of carrier).

Figure 4.3 shows the UART communication between probe and base following this encoding scheme.

4.2.2 Base - Jetson Nano - Touch Display

An UART communication protocol has also been configured between the base MCU and the Jetson Nano as well as between the Jetson Nano and the Touch Display. The processors at each side of the interconnection within these chains must manage the respective UART peripherals to ensure effective communication. The same common setting of 8 data bits, no parity and 1 stop bit (8N1) has been used, but this time at a baudrate of 115200 bps.

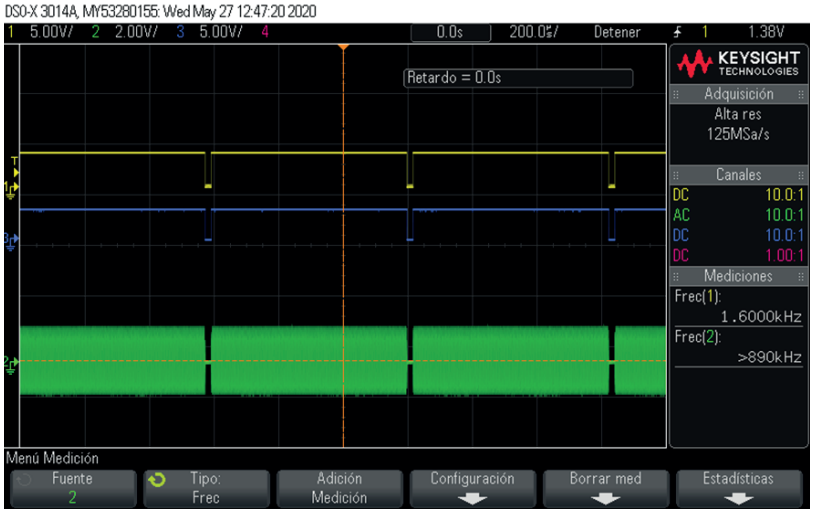


FIGURE 4.3: Example of probe-base UART communication using OOK modulation over the DC power line. The following signals are shown highlighted in color: (yellow) UART communication signal transmitted; (blue) UART communication signal received and; (green) carrier.

Hardware flow control option is again disabled. Data exchange has been configured in non-blocking mode to trigger an interruption each time a data reception is completed.

4.2.3 Jetson Nano - Pulser-Receiver

A 100 Mbps full duplex Ethernet connection is required to communicate the pulser-receiver and the Jetson Nano. Proper network configuration should be defined according to propietary pulser-receiver specifications. Specifically, a Transmission Control Protocol (TCP) port is used for the configuration of the pulser-receiver from Jetson Nano and a UDP port is used for data reception to ensure higher transfer rates of ultrasound data.

4.2.4 System integration

This heterogeneous computing platform consist of several resources that need to be exploited efficiently to ensure real-time operation and system responsiveness. The main application program (Jetson Nano) is responsible for managing the diverse set of event-triggered tasks from the ultrasound system to the probe passing through the base to the touch display. One of the main challenges consists in the global concurrent management of events with minimum latency, on the different processors. A multi-threading scheme is

implemented in the application software to achieve the required functionality and performance in real time. Figure 4.4 shows the system execution graph that always begins from the main thread. This thread is effectively used to bootstrap the initialization of four threaded controllers to manage the AI tasks and the rest of the modules outside the Jetson Nano (probe through base MCU, pulser-receiver and touch display). In this way, a specific control structure running on an independent thread can effectively manage any particular instance of the system.

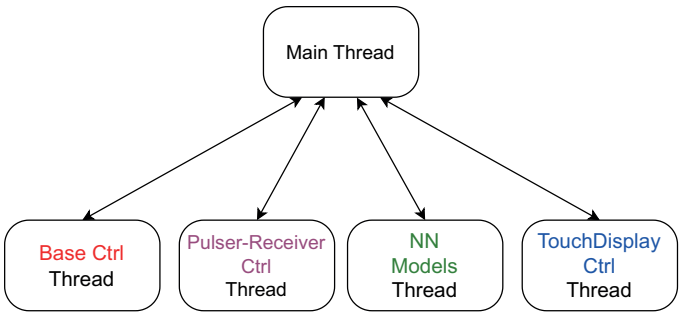


FIGURE 4.4: Multi-threading scheme for the CPU application

To ensure effective communication between each thread on the application software and the corresponding subsystem, a frame exchange approach is followed. Figure 4.5 shows the frame exchange routine on each subsystem and in the related threaded controller on the application software. While this routine can vary on each specific case, the procedure presented is the general approach. This involves establishing proper communication protocols and module interfaces.

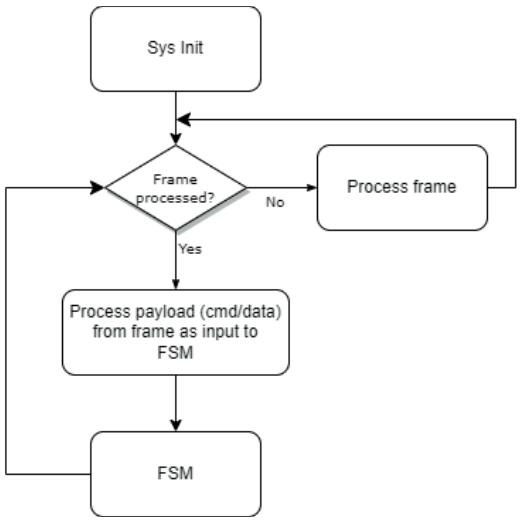


FIGURE 4.5: Frame exchange routine

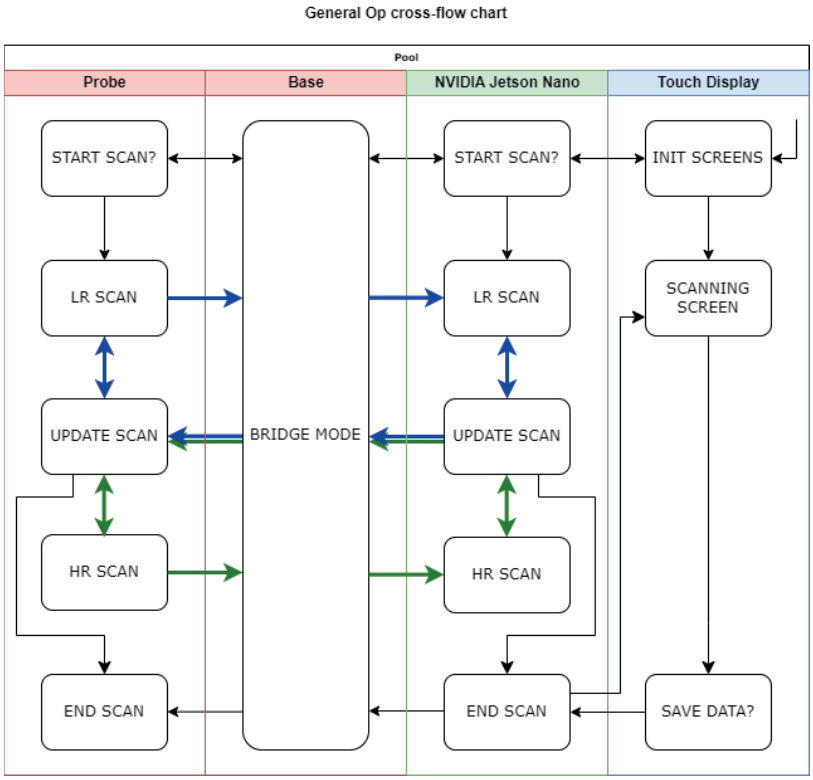


FIGURE 4.6: Interaction overview diagram between system modules.

Received frames are buffered on each subsystem so that they can be processed in order even if they are received during the processing of another. This strategy removes the possibility of losing consecutive frames received in a interval less than the processing time of a frame. Buffered frames are processed on a round-robin basis to generate the input conditions to an Finite State Machine (FSM) (see Figure 4.6). Specific functionality is provided depending on the current state and transitions to a new state when necessary. State management tracks the current state, allowing the program to respond to user input or system events according to the case.

Particularly, the ability to concurrently execute multiple threads on the Jetson Nano, requires a complex state machine on the main thread of the application software for managing all interactions of the data path with the other threads that control the different subsystems.

The event-driven nature of embedded systems means that control flow will change often and unpredictably. A successful system should enable transferring control between processes while minimizing the overhead of these transitions. Additional software is required to arbitrate the desired event source. Each threaded controller context does not have direct access to any other except to the main thread. Data path resources for sharing

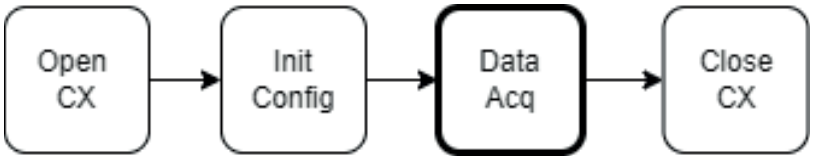


FIGURE 4.7: Control chain for data acquisition from the pulser-receiver: (1) open connection, (2) initial configuration, (3) data acquisition and (4) close connection

data with the main thread are provided for low-latency response to dynamic events. A shared memory model provides communication channel for passing information between threads.

4.3 Ultrasound data management

Communication with the Jetson Nano is established through Ethernet connection. This includes the transference of ultrasound data samples from the pulser-receiver to the Jetson Nano. On the other way, the Jetson Nano controls the operation of the pulser-receiver, as well as sets its configuration parameters, which ultimately impact the image quality.

4.3.1 Data acquisition

The first step for accessing the pulser-receiver from the Jetson Nano is to open an Ethernet connection. When the two devices are linked, predefined settings (for example, emitter/receiver connectors, the acquisition trigger mode, etc.) are uploaded to the pulser-receiver during initialization (this will be covered in the next Section 4.3.2). Then, the pulser-receiver is ready to perform the acquisition of ultrasound data (bold box in Figure 4.7). Once the acquisition is finished, the communication with the pulser-receiver is closed to release its resources. Figure 4.7 depicts the control chain for data acquisition from the pulser-receiver.

In particular, acquisitions can be triggered by software or by an external input signal, besides other options not suitable for this application. For each acquisition mode, a custom *Data Acq* control block must be implemented.

Software trigger mode

In a first approach, A-scans were acquired using software trigger for which a specific *Data Acq* control block was implemented, as shown in Figure 4.8.

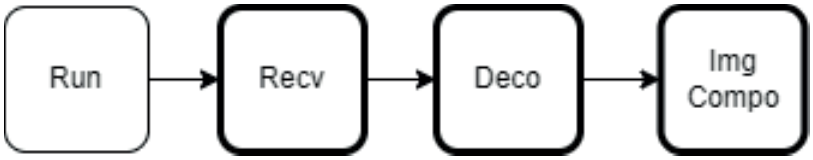


FIGURE 4.8: Control block for acquisitions triggered by software, consisting of: (1) *run* order transmission, (2) UDP data reception, (3) frame decoding and (4) image composition.

To initiate any acquisition sequence, the *run* order must be sent to the pulser-receiver through the TCP port. Measurement results are arranged in frames by the pulser-receiver, typically providing the processed A-scan together with other information related to the reading. Ultrasound data is received on the UDP port of the Jetson Nano in data blocks composed of several frames. Then, the application software decodes the different fields of information and extracts the A-scan data. Finally, ultrasound images are created by assembling sets of successively scan lines, one after the other.

Data acquisition of scan lines must be aligned with the mechanical movement of the transducer to ensure that the data is captured with lateral coherence. Accordingly, a notification frame was sent from the probe to the Jetson Nano just before starting to move the scan motor. Considering the time of arrival of the frame to the Jetson Nano, a delay was required before starting to move the motor. Then, the Jetson Nano starts triggering acquisitions by software, at the same frequency as the motor steps, using timing control mechanisms. However, as shown in Figure 4.9, proper alignment between pulse train that triggers the scan motor steps and the firing events of each pulse-echo process could not be ensured using this approach. In addition, once the acquisitions began, it was not possible to guarantee that they would be performed at equally spaced intervals. This was because the acquisition periods were managed by timers that depend on how the operating system was managing its resources.

External trigger mode

Hence, to ensure that ultrasound data is captured accurately, acquisitions should be triggered at specific intervals aligned with the scan motor steps. The pulser-receiver has an external signal input for synchronizing the acquisitions and conforming B-scan images. In this second approach, the pulser-receiver has been configured, during the initialization process, to start acquisitions from an external trigger. The input signal to the driver that controls when the scan motor takes a step, has been passed through the probe cable

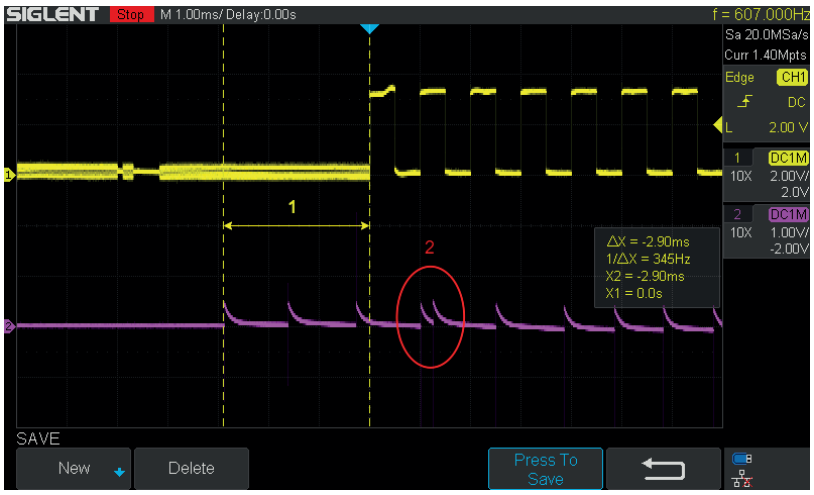


FIGURE 4.9: (1) Misalignment between the pulse train that triggers the scan motor steps (yellow waveform) and the firing events of each pulse-echo process (purple waveform). (2) Firing events are not equally spaced in time.

and connected to the external trigger input on the pulser-receiver. Referred as *Sync* in Figure 3.2, it is responsible for triggering the steps of the scan motor at the time each pulse-echo firing event is started. Therefore, the *Data Acq* control block remains as shown in Figure 4.8, but without requiring *run* orders to be send to the pulser-receiver to start the acquisition sequence (boxes not in bold). As a result, Figure 4.10 shows the pulse train that triggers the scan motor steps, which are now precisely synchronized with the firing events of each pulse-echo process. This tight integration minimizes communication delays and enhances overall system performance.

4.3.2 Configuration parameters

During the initialization process, the pulser-receiver is loaded with predefined settings from a configuration file generated by an application software from the manufacturer. The pulser-receiver is configured with one channel, assigning one connector for emission of the pulse and other connector for reception of the signal. Recall that a preamplifier is used to boost the signal from the transducer on the probe to the receiver. The configuration parameters are set for the channel used, including the emitter/receiver connectors, receiver gain, acquisition window, pulser parameters, average, designed filters, etc. Most of these parameters can be changed during operation of the device.



FIGURE 4.10: Synchronism between the pulse train that triggers the scan motor steps (yellow waveform) and the firing events of each pulse-echo process (purple waveform).

The application software allows the user to configure the acquisition parameters from its user interface. In general, a specific panel has been developed to interact with the configuration parameters. When a control associated with a given parameter is actuated, an event related to a corresponding change is generated. This event is addressed during the *UPDATE SCAN* stage (see Figure 4.6), where a signal is sent to the respective threaded controller that manage the pulser-receiver. This control structure handles it as a slot, and the parameter is written to the specific register of the pulser-receiver following its proprietary protocol. Once the parameter has been updated, the register is read to verify that the operation was performed properly. Using another *signal-slot* connection, the read parameter is sent back from the threaded controller to the main thread, where it is displayed on the screen. This verification step ensures that the configuration on the screen is the one actually configured in the pulser-receiver. The ultimate validation of the configuration parameters is done through direct measurement using an oscilloscope.

Reception

The receiver has a linear amplifier with a dynamic range of 60 dB. Accordingly, a gain control is added which causes a uniform amplification of all returning echoes regardless of the depth of their origin [49]. This control is directly responsible for the overall brightness of the image. This gain is achieved with a 48 dB linear amplifier and a +12 dB stage which is activated if the desired gain is greater than 48 dB and less than or equal to 60 dB.

Beyond the 60 dB, the gain is digital, with a total gain of up to 100 dB. A programmable -20 dB attenuator can also be enabled in the receiver path. The acquisition delay can be configured between 0 and 26214 μs. The acquisition time is set by the number of samples acquired (*SCAN_LENGTH*), taking into account that the relationship is given by 4.1:

$$Acq_time = \frac{SCAN_LENGTH}{f_s} \tag{4.1}$$

, where f_s is the sampling rate. The acquisition time can be configured from 0 to 163 μs.

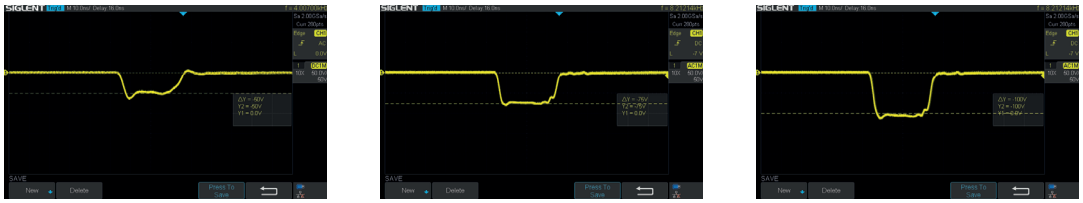
Transmission

The pulse applied to the transducer can be adjusted by means of a pulser control, thereby regulating the sound output from the transducer. Specifically, the excitation pulse of the pulser-receiver is a negative square pulse, which can be set to: -20 V, -30 V, -50 V, -75 V, -100 V, -125 V, -150 V, -200 V, -300 V and -400 V. Figure 4.11 shows representative measurements of the emitted pulse at -50 V, -75 V and -100 V. The stronger the pulses going into the body, the stronger the returning echoes, which in turn creates a overall brighter picture [49]. The pulse width can be set to values between 20 ns and 1000 ns. Figure 4.12 shows representative measurements of the emitted pulse with a width of 20 ns, 25 ns and 30 ns. The pulses number can be set to values between 1 and 255. Figure 4.13 shows representative measurements of the emitted pulse with a number of 1, 2 and 3 pulses.

Digital Signal Processing

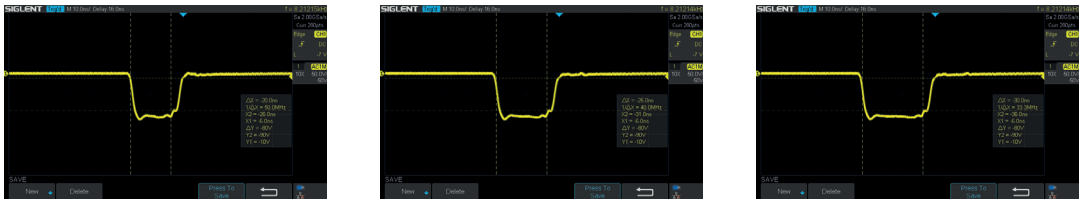
Signal processing capabilities are available at the pulser-receiver for operations such as averaging echoes over several cycles, band-pass filtering and accurate envelope extraction. This processing is found useful to enhance the obtained images.

The number of transmission cycles can be changed to more than one, resulting in a burst whose echoes can be averaged to obtain each A-scan. This number of cycles or average number (not to be confused with the pulses number parameter) can be set to the powers of 2 between 2 and 256. The repetition frequency of the transmission cycles can be set via the PRF configuration between 1 Hz and 20 kHz. Figure 5.8 shows representative measurements for 4 cycles transmitted (of one pulse each) with a PRF of 10 kHz, 15 kHz and 20 kHz respectively, whose echoes would be averaged.



(A) (B) (C)

FIGURE 4.11: (a) Pulse amplitude = -50 V; (b) Pulse amplitude = -75 V; (c) Pulse amplitude = -100 V



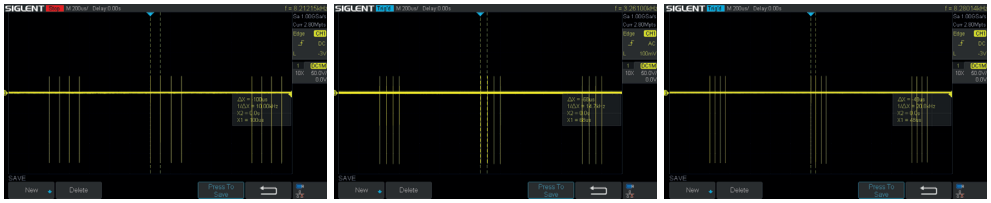
(A) (B) (C)

FIGURE 4.12: (a) Pulse width = 20 ns; (b) Pulse width = 25 ns; (c) Pulse width = 30 ns



(A) (B) (C)

FIGURE 4.13: (a) Pulses number = 1; (b) Pulses number = 2; (c) Pulses number = 3



(A) (B) (C)

FIGURE 4.14: (a) PRF = 10 kHz; (b) PRF = 15 kHz; (c) PRF = 20 kHz

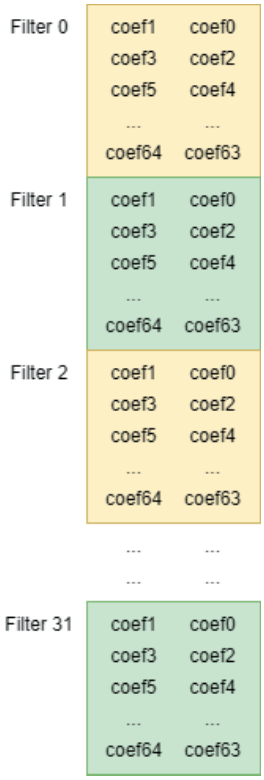


FIGURE 4.15: Memory space allocated for filter coefficients in the pulser-receiver.

Linear filtering is an essential function to reduce unwanted noise. FIR filters have linear phase and provide cut-off frequencies that can be arbitrarily defined within the *Nyquist* band. At sufficiently high order, the passband response can become flat and the transition bands narrow, with high attenuation at the band-stop.

The pulser-receiver has been enabled to program custom 63-coefficient FIR filters by loading the corresponding coefficients into a memory space allocated for this purpose in the pulser-receiver (see Figure 4.15). The filter coefficients must be calculated in advance by the user for the selected cut-off frequencies. Then, they are stored in an external file, which is read by the application software during the initialization process of the pulser-receiver. Any filtering function can be implemented, simply by reprogramming the set of coefficients.

This memory space allows to store up to 32 filters. To select a filter, it is necessary to indicate the corresponding offset within the memory space where the coefficients are located. In practice, by means of a drop-down in the configuration view, a filter can be selected from those initially loaded.

The scan lines (A-scan) can be collected as RF data acquired by the channel from the pulser-receiver, or as video data, from the envelope obtained

after applying a Hilbert transform to this RF signal. Video image data is often more readily available, particularly in a clinical setting. However, most information is available from the RF ultrasound signal, which typically is not available in commercial machines. Lastly, contrast resolution may be enhanced at various stages in the image processing, to improve the ability to distinguish between different echo amplitudes of adjacent structures

Appendix A presents the application GUI, in which the functionalities described above are compressed into a user-friendly platform. Through this GUI, users can intuitively navigate and interact with the application, making it easier to utilize the advanced capabilities and perform various tasks efficiently. This appendix includes detailed screenshots and annotations to illustrate how each function is integrated, showing the design and usability of the application.

Initial configuration of acquisitions

When sequential scan lines are acquired across the body and composed together, a high spatial resolution 2D B-mode image can be obtained. Images are displayed on the screen as sequential frames over time. As shown in Figure 4.16, each frame is created from repeated pulse-echos that form scan lines (A-scan) every 1 ms. Ultrasound images were obtained by sets of 736 scan lines. Therefore, a B-mode image requires 736 ms in total to be generated. Scan lines are acquired during 16 μs with a 100 MHz sampling frequency, resulting in a total of 1600 samples acquired per scan line. The corresponding sampling period of 10 ns can enable an axial resolution of up to 7.5 μm. For a speed of sound in the tissue of 1500 m/s the scan length is equivalent to 12 mm. An acquisition delay of 16 μs was set to keep the 1.5 mm length focal zone approximately in the center of the acquisition range.

Lateral resolution of the composed image depends on the distance between scan lines. This is controlled by the step size configuration on the scan motor during acquisition. In general, the whole acquisition sequence does not change, including the number of scan lines. By default, the motor step size is 0.45^o, corresponding to a distance of 15.7 μm (default lateral resolution), hereafter referred to as HR. If an area of interest is found in the CSF, the resolution can be increased by reducing the step size by one eighth, hereafter referred to as HHR. This way, the arc path is reduced while maintaining the same number of scan lines, as can be shown in Figure 4.17. This higher lateral resolution can reach up to 1.96 μm step size.

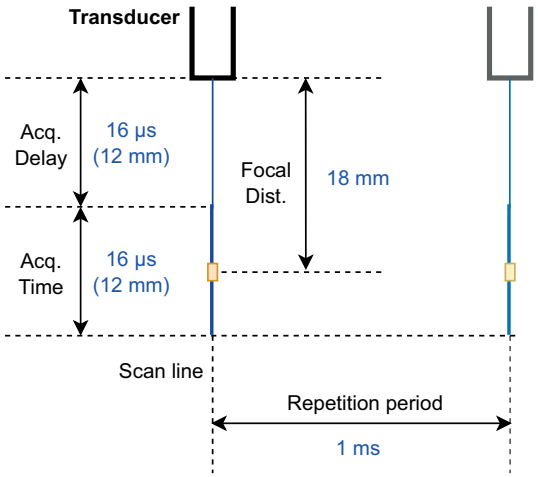


FIGURE 4.16: Receiver configuration to select the acquisition range of the returning echo, from which each A-scan (scan line) is obtained. This configuration ensures that the focal zone (yellow square) lies in the center of the acquisition range. Each frame is created from 736 scan lines acquired consecutively every 1 ms.

Such a data-intensive system allows to store up to 100 images in a circular buffer, thereby always having the last 100 images captured. At the end of a scan this image buffer is saved for further analysis. In addition, configuration parameters are recorded for each image in an external file. This process ensures that images are associated with its specific configuration parameters, allowing for detailed tracking and analysis of the conditions under which each image was captured. In general, this is sufficient to allow experimental investigation of this novel application, which will be described in the following chapters.



(A) (B)

FIGURE 4.17: (a) HR scan path vs HHR scan path; (b) HR img vs HHR img.

4.4 AI at the edge

The measurement of CSF WBC concentration from the high resolution B-mode images is key to the diagnosis of meningitis. This is why, a DL model was developed by [67] to classify (externally) CSF patterns according to WBC concentration from the images obtained with the platform. Thereby, each single image is given a probability of belonging to either the meningitis and the control classes. This model is based on the ResNet50 architecture initialized with pretrained weights [68]. Pytorch was the framework used during the training phase (specifically the Python interface) on a NVIDIA GeForce RTX 3090 GPU.

After the model was trained and optimized to produce accurate results, a file was obtained with the weights and activation functions that encode the network topology. Thus, the model need to be transformed and optimized according to the specific embedded GPU architecture of the Jetson Nano. First, the Pytorch model was converted to Open Neural Network Exchange (ONNX), an open format for representing machine learning algorithms. ONNX allows moving easily NN descriptions between different frameworks, some of which may be more suitable for specific phases of the development process. In this case, Pytorch was selected for fast training, taking advantage of the flexibility to work with network architectures and TensorRT was used to port the network for inference on the specialized hardware of the Jetson Nano.

TensorRT framework enables the efficient deployment of this pre-trained model on the GPU accelerator of the Jetson Nano. In general, this kind of NN deployment frameworks are intended only for inference (not for training) [69]. This deployment framework allows to introduce optimization methods, which focus on reducing computing requirements of deep learning models towards resource-constrained platforms. The deployment framework is very important as it marks the success of the NN deployment or its total lack of applicability [69].

After parsing the ONNX model, a TensorRT engine is generated from this network, optimized for the target hardware platform. This engine is loaded into the application software from a thread raised specifically to handle the executable contexts of the DL models (as described in Section 4.2.4). Then, memory was allocated based on the dimensions of the inputs and outputs of the model. The pre-processing performed on the images during the training phase must be implemented again to prepare captured data for inference, but

using only the available C++ libraries. The cropped 145x390 images are converted to 3 channels, uploaded to the GPU and then, normalized (dividing pixel values by 255, subtracting the mean and dividing by standard deviation). Once the input data is prepared (batch of one image), it is passed to the network to run the inference using the GPU hardware. As a result, a tensor is obtained with a confidence value of belonging to the meningitis and control classes. The post-processing step of the data obtained must also be replicated to obtain readable data. This step can be executed from the CPU due to its low computational requirements. A *sigmoid* function is applied to provide the probabilities for each class (in the range 0 - 1), i.e. control or meningitis. Finally, once the classification has been completed, the used memory is released.

Chapter 5

Tests and results

This chapter describes the optimization process and evaluates the results of the high-resolution ultrasound system through *in vitro* and *in vivo* tests. First, Section 5.1 presents the setup prepared for the *in vitro* experiments, highlighting the main elements that integrate the testbench, as well as the test procedure. Then, the experimental tests are presented. Section 5.2 is oriented to obtain the ultrasound configuration that maximizes image quality while maintaining the safety limits. Next, Section 5.3 evaluates the resolution achieved by our platform and provides an analysis of the target components under observation. Finally, an *in vivo* assessment of the patient classification model according to the CSF image examination is shown in Section 5.4. It includes the performance analysis of this solution on the embedded platform to demonstrate the feasibility of the tool in a clinical setting.

5.1 Experimental setup

An experimental setup is designed to test the device in order to evaluate the feasibility of the proposed solution. Figure 5.1 shows the probe held with a bracket with 2D versatile movement that allows the transducer to be oriented vertically downwards against the sample container. The sample container is placed on a elevating platform that allows it to be brought close to the transducer. At high resolution, any significant human movement compromises the quality of the acquired image. Once the sample container is fixed at a contact distance to the transducer, depth adjustment is mechanically controlled in the probe by the motors.

Before the experiments, the pulse-echo ultrasound configuration is characterized using a flat brass reflector placed in front of the transducer, being both immersed in a water bath. The distance between the transducer and the reflector is adjusted around the nominal focal distance (18 mm) to obtain the

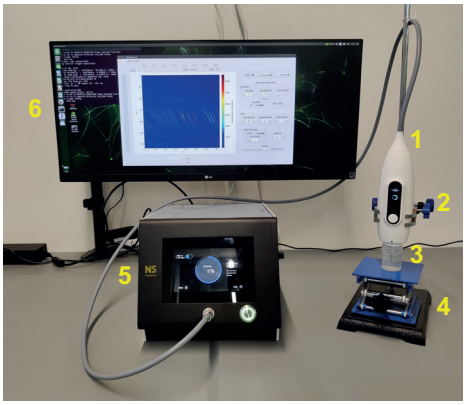


FIGURE 5.1: Experimental setup composed of: (1) ultrasound probe, (2) bracket, (3) sample container, (4) elevating platform, (5) base module, and (6) external monitor.

maximum intensity. Figure 5.2 shows the pulse-echo response measured for the 20 MHz transducer.

5.1.1 Sample container

The white blood cells inside the CSF are simulated with particle suspensions in ultra pure water (Milli-Q), under different concentrations relevant to meningitis diagnosis (7 to 650 pp/μL). Polystyrene particles with a mean diameter of 7 μm are used to mimic approximately the dimensions of WBCs [70, 71]. It is important to note that the diameter of the particles is below half the transmitted wavelength that corresponds to the acoustic diffraction limit. These samples are characterized at the analysis laboratory in Barcelona Scientific Park (Barcelona Spain) using the Fuchs Rosenthal method for concentrations lower than 200 pp/μL and the Neubauer method for concentrations equal or higher than this value. The experiments are performed just

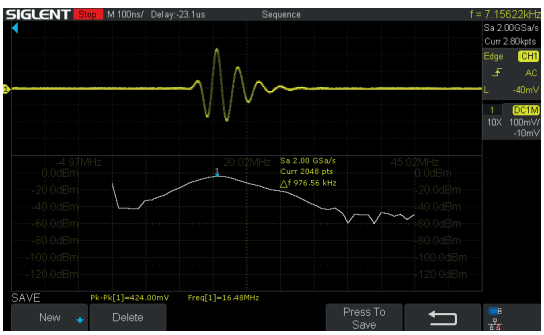


FIGURE 5.2: Measurement of the pulse–echo impulse response and spectrum of the 20-MHz transducer.

TABLE 5.1: Initial configuration of acquisitions.

Configuration parameter	Value
Acq. delay	16 μs (12 mm)
Acq. time	16 μs (12 mm)
Sampling rate	100 MHz
Sample number	1600 samples

after sample preparation, in order to prevent the particles from settling on the bottom or walls of the container.

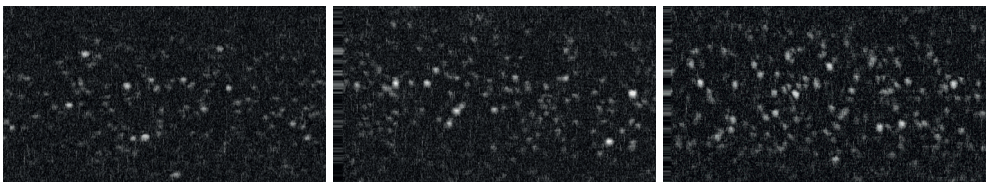
Two specific setups have been mounted to conduct our experimental tests. The **setup 1** is the simplest one, based on a container with the sample at various concentrations. The **setup 2** is a phantom based on the anatomy of a neonatal head, embodied in a container as in the previous case. This emulates a tube section from the fontanelle cap to the cortex of the brain. The fontanelle is modeled using a 4 mm thick tissue-mimicking layer made of polyvinyl alcohol (PVA)-based hydrogel [72]. The pulse-echo total attenuation of this layer at 20 MHz is 6.3 dB, similar to the real fontanelle [15]. The zone between the fontanelle cap and the cortex corresponds to the CSF simulated with the sample solution.

5.2 Optimization of ultrasound configuration

The configuration parameters of the ultrasound platform directly influence the image quality. Adjusting these settings properly is essential to ensure that images are displayed optimally while complying with the acoustic safety limits. Accordingly, the system can be adapted to patient-to-patient variations and to different clinical applications on serous body fluids. In addition, the quality of the images is critical to the performance of the neural network models in computer vision tasks [73].

Several *in vitro* experiments have been performed using the setup 2, with a concentration of 84 pp/μL to evaluate the influence of each configuration parameter on the resolution and quality of the images, with a focus on improving the visualization of white blood cells. The preliminary configuration defined in the previous chapter (Section 4.3.2), is used as the starting point for the experiments (summarized in Table 5.1).

First, the gain has been adjusted over the entire image to compensate the attenuation caused by the fontanelle, the main obstacle for ultrasound imaging in this application. Specifically, the gain was increased until the



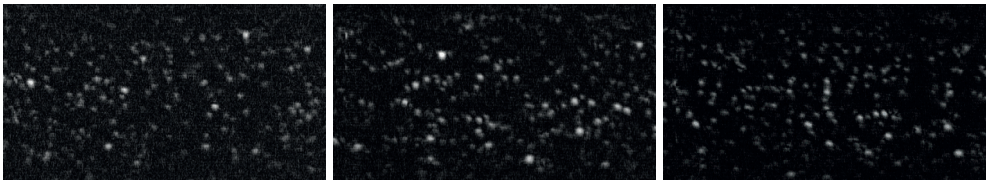
(A) (B) (C)

FIGURE 5.3: B-mode images (video-mode) obtained when the transducer is excited with: (a) -50 V, (b) -75 V and, (c) -100 V single-squared pulses of 25 ns wide. Echo signals are amplified 32 dB before being input into the receiving stage. A second amplification gain in the range 35 dB is further applied.

image definition stopped improving with it, always avoiding saturation. Finally, the amplification level has been fine-tuned to 35 dB, whereby the image brightness is equalized for the pulse amplitude range to be tested (50-100 V). As expected, when images are over-gained or under-gained, the resolution worsens [48].

From the transmitter side, the pulser configuration has been manipulated to produce a pulse that optimally matches the impulse response of the transducer element. As the working frequency of the transducer is 20 MHz, a pulse width of 25 ns is set to form a square wave with a period of twice this value (duty cycle = 50 %). A single pulse is used in order to minimize the spatial pulse length and obtain the best axial resolution. Transmitted pulses should have enough amplitude to compensate for the aforementioned tissue losses with an adequate SNR. However, the amplitude of the output signal must be maintain within clinical safety limits during operation. Thus, various pulse amplitudes have been tested (-50 V, -75 V and -100 V) taking into account that this voltage should be set as low as possible to achieve the resolution required to distinguish the WBCs within the CSF.

Figure 5.3 shows the resulting B-mode images (video-mode) obtained when the transducer is excited with -50 V, -75 V and -100 V single-squared pulses of 25 ns width. Note that echo signals are amplified 32 dB (by the preamplifier) before entering the receiving stage. A second amplification gain in the range of 35 dB is further applied, as mentioned before. Increasing output intensity, as well as increasing gain, will not improve image definition. On the contrary, the detail in the rendered images degrades and may increase artifacts, such as reverberation echoes [49]. Since the energy is determined by the area under the curve, when more pulses are transmitted, the amplitude of the pulses will be lower for a given amount of energy [61], and the resolution would be compromised.



(A) (B) (C)

FIGURE 5.4: B-mode images (video-mode) obtained by averaging returning echoes over (a) 2, (b) 4, and, (c) 8 transmission cycles to get each A-scan that form the image, using a 20 KHz PRF. The transducer is excited with a -75 V single-squared pulses of 25 ns wide.

Several digital signal processing methods have been selected and tested to improve the information content of each A-scan that later composes the ultrasound image. They are executed on the pulser-reciver hardware, thus allowing a higher throughput than in the case they run in the application software.

To overcome the effects of impulsive noise, B-scan images are created by averaging the echoes of several cycles. This process requires several cycles of ultrasound transmission along the same scan line, whose repetition frequency is controlled by the PRF. For each of the pulse amplitude settings, several experiments have been performed using different average numbers.

Figure 5.4 shows B-mode images (video-mode) obtained after averaging returning echoes over 2, 4, and, 8 transmission cycles to get each A-scan that form the image. The PRF is set at 20 kHz, the maximum supported by the pulser, to ensure that the multiple cycles are repeated as close to each other as possible. The transducer is excited with a -75 V single-squared pulses of 25 ns wide for these experiments.

However, it is important that the time between transmission cycles is long enough to allow the returning echoes to reach the transducer before the next cycle is emitted. When a transmission cycle occurs too early, the overlap with the returning echoes may result in erroneous data, as shown in Figure 5.5. For reference, a PRF from below 1 kHz to above 10 kHz is required for diagnostic ultrasound [49]. Finally, with an average number of 4, a sufficiently high image quality has been obtained without having to further increase the number of transmission cycles to get each A-scan that form the image (more details in in Section 5.3.3).

Linear filtering is performed by means of a 63-coefficients FIR filter, embedded in the pulser-receiver. This way, the SNR is improved while keeping the axial resolution of the transducer. Several FIR filters have been designed

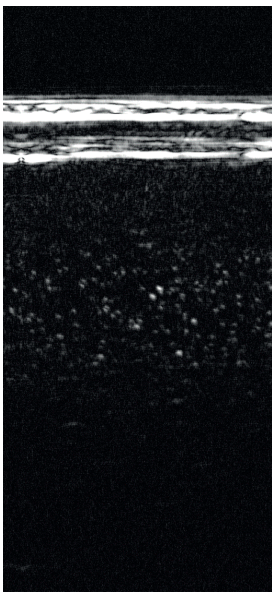


FIGURE 5.5: B-mode image obtained by averaging returning echoes over 4 transmission cycles to get every A-scan that form the image, using a 27 kHz PRF. The transducer is excited with a -75 V, 25 ns wide single-squared pulses.

in MatLab, adjusting the bandwidth to that of the transducer (10 MHz - 30 MHz). Figure 5.6 shows the magnitude of the frequency response for selected FIR filter with a passband between 10 MHz and 30 MHz and a sampling rate of 100 MHz. The classical techniques for designing FIR filters are considered: windowing, frequency sampling, McClellan transformation and least squares [74].

The least-squares linear-phase FIR filter has been chosen because it produced less ripple in the attenuation band. The ratio of the pass-band to the stop-band attenuation is above 80 dB, as shown in Figure 5.7. This FIR filter is optimal since minimizes the maximum error at the desired frequency band (as well as the one based on the Parks-McClellan algorithm).

5.2.1 Discussion

In this experiments, we have evaluated various configurations of the pulses that excite the transducer. Specifically, the pulse amplitude is gradually increased from -50 V to -100 V in -25 V steps (according to the characteristics of the pulser) until good quality is obtained for the images, according to the ALARA principle. However, we have to take into account the output power to ensure meeting the regulatory limits to minimize the risk to the patient.

To verify that extent, we rely on the acoustic output measurements of the focused transducer we use, which were performed by the National Physical

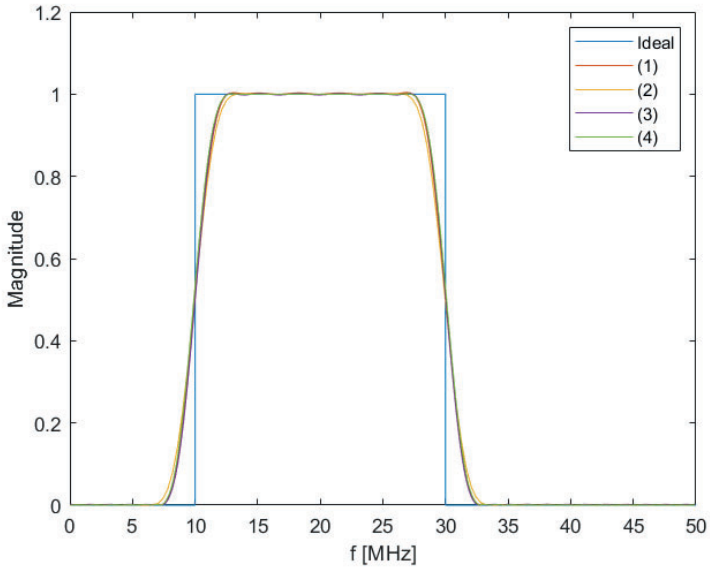


FIGURE 5.6: Comparison of magnitude frequency response of designed FIR bandpass (10 MHz - 30 MHz) filters based on: (1) windows (Hamming), (2) frequency sampling, (3) Parks–McClellan transformation and, (4) Least-squares.

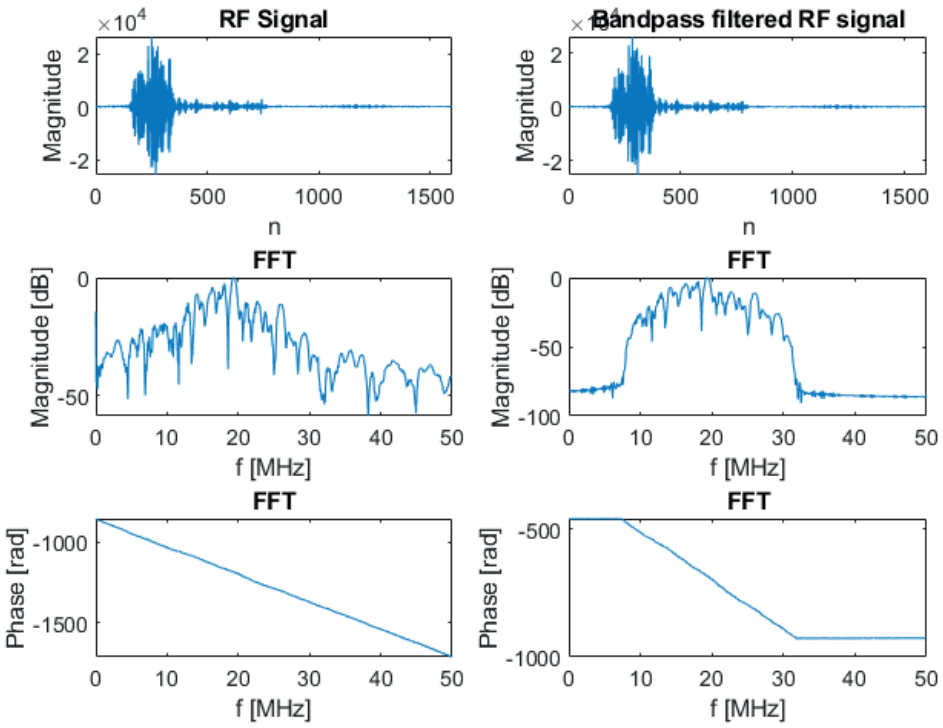
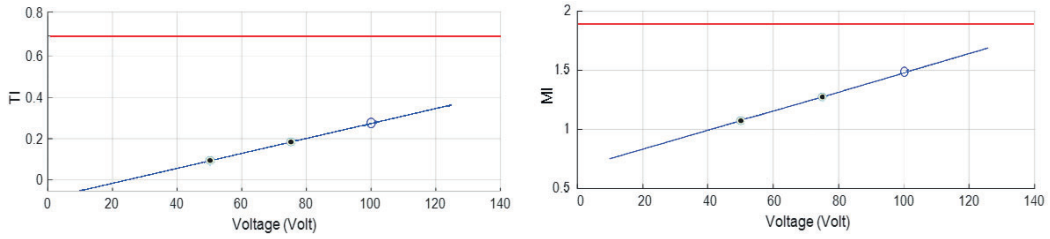


FIGURE 5.7: RF signal filtered by a least-squares linear-phase FIR filter between 10 and 30 MHz.



(A) (B)

FIGURE 5.8: TI (a) and MI (b) measurements (marked -●-) according to pulse amplitude configurations of -50 V and -75 V. New data points (marked -○-) corresponding to -100 V are obtained by linear interpolation. Red lines indicate the FDA recommended limits of TI < 0.7 and MI < 0.9.

Laboratory (NPL) in 2019. From this ultrasonic field characterization, the TI and MI have been measured for each pulse amplitude configuration. Figures 5.15a and 5.15b show the results obtained of TI and MI respectively, for pulses amplitudes of -50 V and -75 V. In both cases, these two points are connected with a straight line to roughly estimate the value corresponding to -100 V.

These measurements are then compared against the safety thresholds recommended by regulatory bodies, in this case, the FDA (See Section 2.5). Results revealed that all the pulse amplitude settings considered complied with the corresponding safety standards for both the TI (< 0.7) and the MI (< 1.9). However, the estimation for -100 V presented a MI value of 1.48 that is close to the recommended limit, indicating the need for careful monitoring (or even adjustment) in clinical settings. Accordingly, the selected -75 V pulse amplitude setting obtains a good enough quality of the captured ultrasound image while reduces the risk to the patient. Table 5.2 shows the ultrasound imaging configuration selected for the meningitis application. This configuration, together with the initial parameters set in Table 5.1, will be used throughout the rest of the thesis.

5.3 Evaluation of system resolution

A definitive demonstration of resolution can be achieved by imaging real features that have already been characterized using a reliable technique, which serves as a ground truth with which to compare. To evaluate the capacity of the proposed solution for imaging white blood cells, *in vitro* experiments using both setup 1 and 2 are conducted under different concentrations relevant to meningitis diagnosis (7-, 19-, 69- and 646-pp/μL). The basic idea

TABLE 5.2: Ultrasound configuration adapted for the meningitis application in which images are optimally displayed while complying with the regulatory safety limits.

Configuration parameter	Value
Gain	35 dB
-20 dB attenuator	disabled
Pulse amplitude	-75 V
Pulse width	25 ns
Pulses number	1
"Average"	enabled (4 transmission cycles)
PRF	20 kHz
FIR filter	Passband (10 MHz - 30 MHz) based on least-squares method
Envelope extraction	enabled (Hilbert transform)

is to evolve from the simple setup 1 to the setup 2 based on the anatomical phantom. Batches of 100 images are acquired for each experiment.

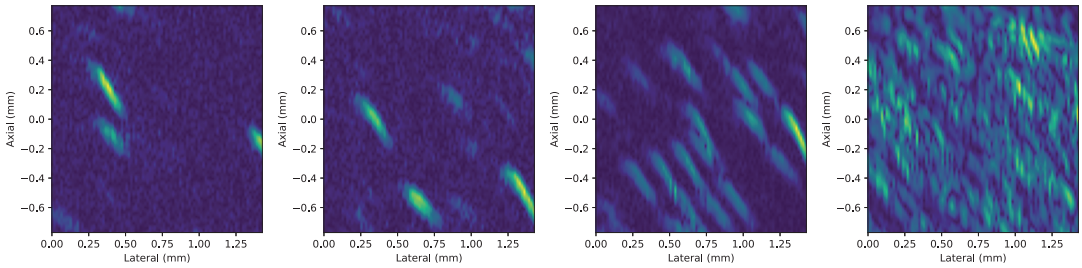
5.3.1 Setup 1

For this experimental setup, the probe is dipped into a ultra pure water suspension with 7-μm-diameter particles (setup 1) with the concentrations mentioned above. The probe is introduced in the container at a minimum depth such that the transducer emitting face is in direct contact with the water. Mechanical alignment is performed via the elevating platform while receiving real-time image feedback from the application software, ensuring to have the focal region inside the area of interest in the liquid.

Figure 5.9 shows representative frames of experimental HR B-mode images (video-mode) obtained from setup 1 for every concentration. Similarly, Figure 5.10 shows the images corresponding to the HHR-mode acquisitions.

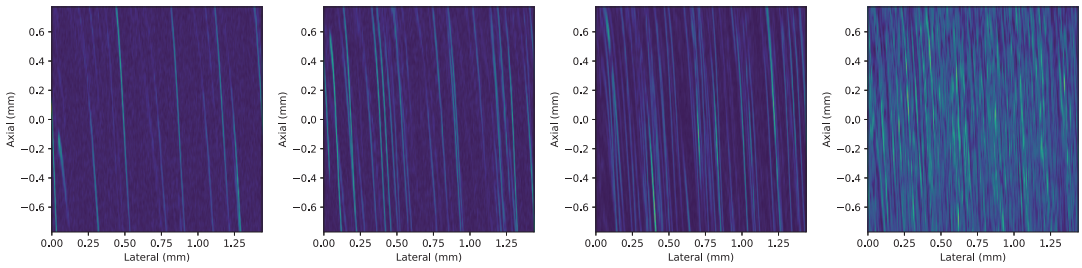
5.3.2 Setup 2

In this case, a coupling gel is applied on the fontanelle cap to facilitate energy transfer. The probe is then lowered into the coupling gel, simulating the proposed mode of operation. Due to the physical fragility of the phantom, the transducer can not contact the fontanelle during scanning but scans through the thin gel layer between the transducer head and the fontanelle cap. It is important to locate the CSF zone inside this model, where the particles are located. To this end, the transducer is moved mechanically using the depth



(A) (B) (C) (D)

FIGURE 5.9: Detail of the HR B-mode images (video-mode) obtained with setup 1 on 7–μm particles suspension under 7-, 19-, 69- and 646–pp/μL concentrations, respectively from left to right.



(A) (B) (C) (D)

FIGURE 5.10: Detail of the HHR B-mode images (video-mode) obtained with setup 1 on 7–μm particles suspension under 7-, 19-, 69- and 646–pp/μL concentrations, respectively from left to right.

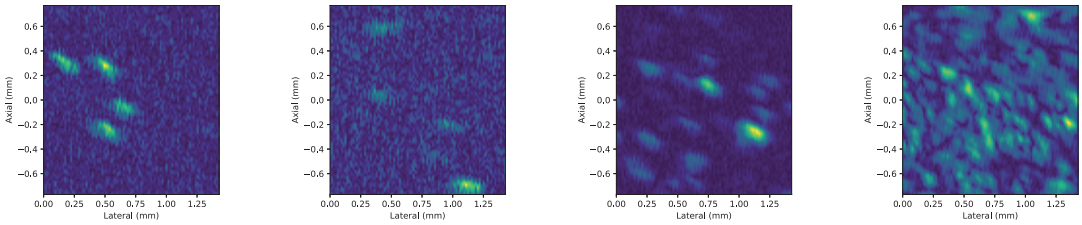
motor in the probe until aligning the area of interest with the focal zone in the center of the image.

Figure 5.11 shows representative frames of experimental HR B-mode images (video-mode) obtained with setup 2 for 7-, 19-, 69- and 646–pp/μL concentrations, respectively. Similarly, Figure 5.12 shows the corresponding images relative for HHR-mode acquisitions.

5.3.3 Discussion

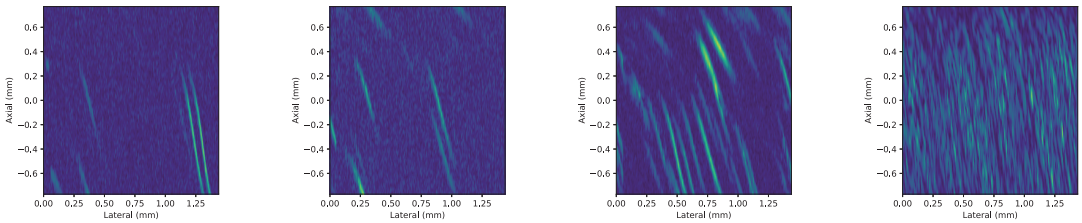
The ultimate measurement of resolution in this application is to distinguish particles from liquid. Experimental results show that the implementation proposed can attain 7 μm particles. In the horizontal band running through the center of the image, where the focal zone is located, the bright traces of the particles can be clearly distinguished from the background. This focusing effect becomes more evident as the concentration increases.

As the concentration increases, it can also be observed that traces of nearby particles can overlap and appear as single particles or clusters in the image.



(A) (B) (C) (D)

FIGURE 5.11: Detail of the HR B-mode images (video-mode) obtained with setup 2 on 7–μm particles suspension under 7-, 19-, 69- and 646–pp/μL concentrations, respectively from left to right.



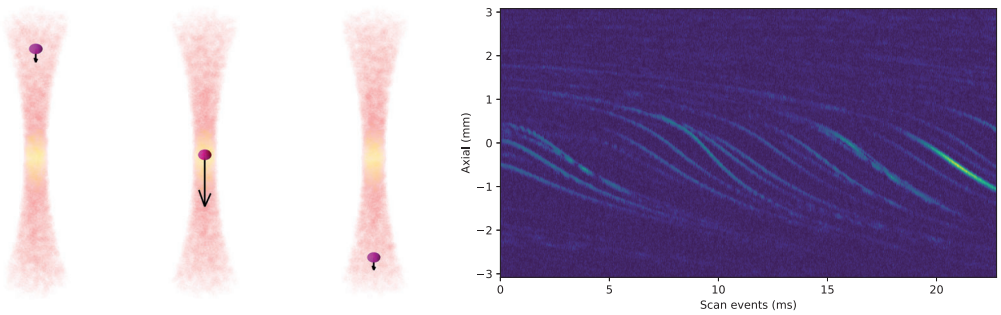
(A) (B) (C) (D)

FIGURE 5.12: Detail of the HHR B-mode images (video-mode) obtained with setup 2 on 7–μm particles suspension under 7-, 19-, 69- and 646–pp/μL concentrations, respectively from left to right.

The superposition of echoes is caused by the proximity between particles beyond the spatial resolution. This effect is due to the fact that the echoes of the particles are larger than the particles themselves. This is a consequence of the wavelength being greater than the size of the cell [15].

It is important to notice that the pulse firings affects the path of the particles as shown in their flow patterns from Figures 5.10a–5.10d and 5.12a–5.12d for HHR scans on both experiments. Figures 5.13a–5.13c depicts how particles are actually pushed down by each repeated pulse-echo used to form a scan line. Since ultrasound images are generated using consecutive scan lines, the motion of particles is translated into the image as the characteristic sigmoid shaped traces observed in Figure 5.13d and others above.

This movement is due to the the ultrasound pressure field produced by the focused transducer that is stronger in the focal zone and may end up moving a particle out of the focal zone after several acquisitions. On the other hand, these movements push new particles to the focal zone. The sigmoid effect at the ends of the traces is due to the fact that, at the ends of the focal zone, the particle receives less pressure, so the displacement effect is less pronounced when composing the image. The acoustic origin of this



(A) (B) (C) (D)

FIGURE 5.13: Difference on the pressure effect of the ultrasound beam on the speed of a particle depending on its location: (a) above the focal area, (b) in the focal area, and (c) below the focal area. This location dependent pressure effect creates a sigmoid shaped trace on the particle trajectories when multiple scans are consecutively shot without moving the scanner head (M-mode, extreme case) (d).

force is observed when the pulse energy and PRF are varied in the vicinity of the particle. This effect is evident in HHR scanning, where the scan lines are acquired closer together to increase lateral resolution. When several acquisitions are obtained and averaged to get every single A-scan at any given position, this effect is even more noticeable when the PRF is increased. This effect support the decision to maintain the average number at 4. The extreme case is achieved by obtaining acquisitions in the same position, without moving the scan motor (M-mode).

As mentioned in Section 3.3.1, this imaging method acquires scan lines to create the image by sending multiple pulses sequentially. Particles move during the data acquisition process. However, the temporal resolution is sufficient to track the resulting particle pattern in the images with lateral coherence.

5.4 On-device evaluation of CSF classification according to WBC concentration

The DL model deployed into the Jetson Nano application is trained to classify CSF patterns according to the WBC values obtained through LPs [67]. To this end, high resolution B-mode images have been collected from patients recruited in three Spanish university hospitals, one Mozambican public teaching hospital and one Moroccan university hospital. Patients are neonates

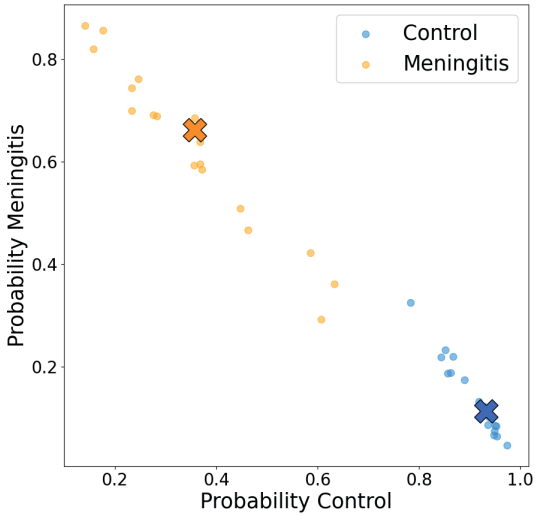
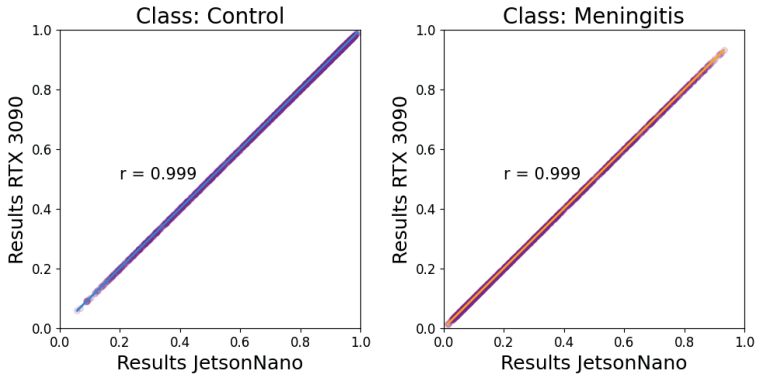


FIGURE 5.14: Example of the probability distribution of the 18 images acquired for two patients. According to the ground truth, controls are labeled in blue and meningitis cases in orange. Each dot shows the probability of each image of belonging to the control class (X axis) versus belonging to the meningitis class (Y axis). The crosses indicate the final classification (median probability) for each patient.

and young infants (<24 months) with an open anterior fontanelle and an indication for LP due to suspected meningitis (LP performed within 24 hours from image acquisition). For analysis purposes, a threshold of more than 30 WBC/μL has been established for positive cases of meningitis. Conversely, controls are defined as patients with a WBC count below the aforementioned threshold. The CSF laboratory-based WBC counting is used as the ground truth data to train and evaluate the DL model.

The process of acquiring CSF images for WBC concentration analysis from the proposed platform consists of several steps. First, a suitable view of the CSF needs be found manually in HR resolution, considering the anatomical characteristics specific to each patient. Images with visible poor coupling should be avoided. Then, lateral resolution is increased in the region of interest and multiple images are acquired in HHR resolution, being 18 images enough to give an accurate prediction. The model is applied to each of the acquired HHR images. With this model, each image obtains a probability of belonging to either the control class or the meningitis case class. The final classification is calculated as the median of the probabilities of all the images. Figure 5.14 shows an example of HHR images from two different patients classified as control and meningitis case, respectively.



(A) (B)

FIGURE 5.15: Performance comparison when running inference of the classification model on (a) NVIDIA GeForce RTX 3090 using CUDA vs (b) GPU accelerator of the Jetson Nano using TensorRT.

5.4.1 Discussion

The performance of the classification model deployed on the device is evaluated at both the individual image and patient level (combining the probabilities of all images). With regard to single HHR image classification, the performance on the platform where the Pytorch model is trained and evaluated (NVIDIA GeForce RTX 3090) using CUDA is compared against that obtained on the embedded computing platform of our platform (NVIDIA Jetson Nano) using TensorRT. The predicted classes match on both platforms with a Pearson correlation coefficient (PCC) of 0.999 (almost perfect correlation), as shown in Figure 5.15.

Since the performances of both systems practically coincide at the individual image level, it is evident that they will be very similar at the patient level. Table 5.3 shows the accuracy, as well as the sensitivity and specificity, achieved by this model at both levels after being evaluated using 1823 HHR test images.

TABLE 5.3: Performance of the classification model of CSF patterns according to the WBC concentration.

	Image level	**Patient level**
Accuracy	82.0 %	94.7 %
Sensitivity	72.2 %	94.1 %
Specificity	86.3 %	94.9 %

Likewise, we have compare the inference execution time on both platforms. The model setup time is not considered, nor any other time related to

image processing. The average time to classify an HHR image is about 2 ms, very similar on the two platforms.

The complete time required to obtain the necessary ultrasound images and provide an estimate based on the WBC count can be derived from the time spent at each step of the procedure. After pressing the start button, the system spends 736 ms to generate every B-mode image, as shown in Section 4.3.2. The routine procedure consist of capturing a certain number of HR images to find the region of interest. Then, 18 HHR images are required to obtain the patient classification, to which the model inference time must be added to obtain a total latency of 738 ms per HHR image. The result is that the entire procedure can be completed in only a few minutes, which is a very satisfactory result according to the current clinical practice. Therefore, this method produces rapid measurements that meet the expected limitations of clinical settings, due to factors such as gravity of the disease and undesirable movements of patients and operators.

Chapter 6

Conclusions and future directions

6.1 Conclusions

A portable platform has been implemented to achieve high resolution ultrasound that allows the non-invasive evaluation of the concentration of WBC in the CSF below the fontanelle of neonates and young infants. In this way, it is possible to confirm or exclude with reasonable confidence the suspicion of infant meningitis. Although ultrasound is considered a safe imaging method, special care has been taken not to exceed the established acoustic safety limits.

This thesis attempts to draw attention to a disease that remains a worldwide burden with devastating consequences, especially for young infants. In response, efforts have been devoted to researching and developing a non-invasive alternative or complement to the traditional methods used to diagnose infant meningitis, such that more sick children can have access to rapid screening methods.

Ultrasound is one of the most widespread imaging modalities in clinics, due to its low cost, portability, and safety. In addition, it is recognized as a form of non-ionizing energy that can be applied in a non-invasive way. These unique features make ultrasound a valuable option with the potential to have a reach beyond that of other imaging tools.

However, conventional ultrasound imaging techniques are limited in spatial resolution to visualize WBC in the CSF. Using high-frequency ultrasound by means of a 20 MHz focused transducer, the spatial resolution has been improved to the point where the backscatter signal of the microscopic WBC can be detected. With a mechanically-driven probe specifically designed for this application, the CSF is scanned laterally at high resolution, allowing a coherent reconstruction of the frames with respect to the imaged area. Several components, both hardware and software, were efficiently integrated into a

single AI-powered solution to enable accurate imaging and CSF analysis according to the WBC concentration.

The optimization process and *in vitro* evaluation of the implemented system were essential to adjust the ultrasound configuration in order to obtain high quality images while complying with TI and MI safety guidelines. With this configuration, direct detection of 7 μm particles in watery suspensions was achieved using a phantom based on the anatomy of a neonatal head. In addition, experimental measurements were conducted to characterize this particles in solutions under different concentrations relevant to meningitis diagnosis. This experiments provide valuable information on the concentration, size or unique flow pattern of such particles that can be directly aligned with those present in white blood cells inside the CSF.

The developed system allows acquiring images with high resolution providing excellent clarity and detail. The high acquisition rate provided by this imaging method has enabled smooth visualization of particle flow inside the experimental setup, which probes the temporal resolving power of this imaging paradigm in depicting flow motion. Thus, the temporal resolution and spatial resolution are closely linked to follow the motion of the white blood cells.

A DL model have been embedded into the platform to classify patients based on CSF patterns according to WBC concentration. Hence, if the diagnostic levels of white blood cells in the CSF are exceeded and a meningeal infection is suspected, treatment can be initiated. The performance of these algorithms running on-device has not been noticeably affected due to the optimization process performed for the specific hardware of this platform. Moreover, local processing contributes to accelerate the results, allowing on-site analysis to be performed in a matter of minutes.

Clinical trials conducted in Spain, Morocco and Mozambique have shown promising preliminary data that demonstrate the potential of the platform. With this device, the diagnosis of infant meningitis can be supported when LPs and CSF analysis are not feasible, as could be the case in resource-poor countries. On the other hand, it would contribute to reduce the indications for LP among patients with a low degree of suspicion, specially in countries with more resources, where complementary test are available. In addition, since ultrasound imaging is non-invasive, the progression of the infection can be followed serially in the patient, with patients serving as their own control. This ability to assess the progression of the infection and the response to treatment non-invasively is a significant advantage of ultrasound.

All this factors could enable a more efficient use of resources and efforts in the plans to defeat meningitis.

To conclude, this thesis has presented a comprehensive approach that establishes a robust and efficient methodology for accurate and immediate CSF analysis, ultimately improving the diagnosis of infant meningitis through an optimized and thoroughly evaluated platform.

6.2 Future directions

Further research and development efforts are warranted to refine the technique, validate its clinical utility, and ultimately improve outcomes for neonates and young infants at risk of meningitis. In this case, as it is a medical device, a strong validation and certification is required to meet the specified requirements.

Future work will focus on improving the ultrasound configuration methods to achieve an optimal balance between safety and image quality. The aim is to dynamically adapt the configuration parameters based on the analysis of the acquired data. In other words, a closed-loop system where feedback information is obtained and the necessary adjustments are applied. Additionally, advanced image processing techniques will be explored to further improve image resolution and ultimately enhance the efficiency and reliability of DL models.

One of the major challenges in high resolution ultrasound imaging is to determine the accuracy of the system. It is difficult to verify whether the observed components have been correctly reconstructed and properly represent the underlying structures. The complexity of biological tissues and the possibility of artifacts or distortions further complicate this verification process. More studies are needed that include extensive testing, comparisons with other imaging modalities, and the development of advanced algorithms to improve reconstruction accuracy.

In addition, much research remains to be done to develop more effective algorithms and models for evaluating WBC concentrations in the CSF using high-resolution ultrasound. This involves not only creating more accurate computational methods for detecting and quantifying cells but also validating these methods against established standards. Such research would need to address challenges such as distinguishing between different types of cells, dealing with varying fluid compositions, and ensuring robust performance across different clinical settings. Progress in this area could greatly enhance

the diagnostic power of ultrasound, enabling more precise and reliable analysis of serous body fluids for medical diagnoses.

In fact, although the primary focus of the device revolves around infant meningitis, this platform can enable the screening and monitoring of other infections in serous body fluids enhanced by the use of advanced algorithms and AI techniques. For example, new research projects have been opened related to other applications such as the screening, diagnosis and non-invasive monitoring of: (i) peritoneal dialysis-related peritonitis and (ii) uveitis.

Appendix A

Application GUI

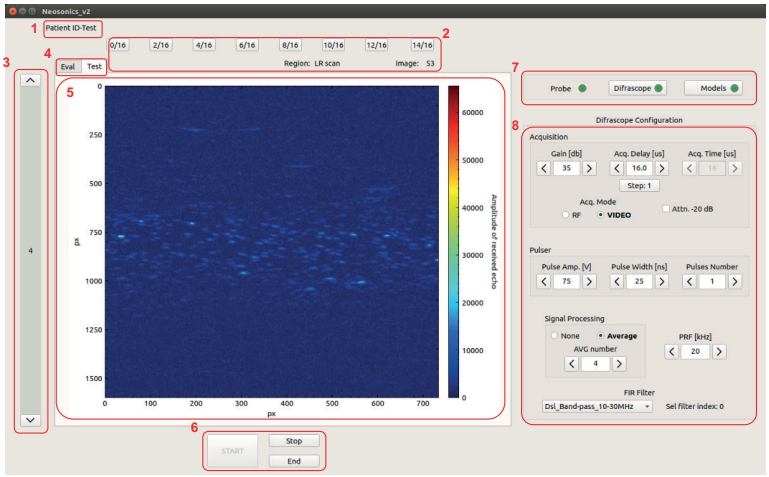


FIGURE A.1: Application GUI from which the system can be controlled in an advanced way, compared to the Touch Display, which is more limited. This GUI is composed of the following elements: (1) patient ID indicator, (2) HHR zone control, (3) focus control, (4) view control, (5) corresponding view, (6) start/end operation control, (7) connected modules indicator, (8) ultrasound parameters configuration panel. This specific case corresponds to the Test view, from where the HHR B-mode image can be observed.

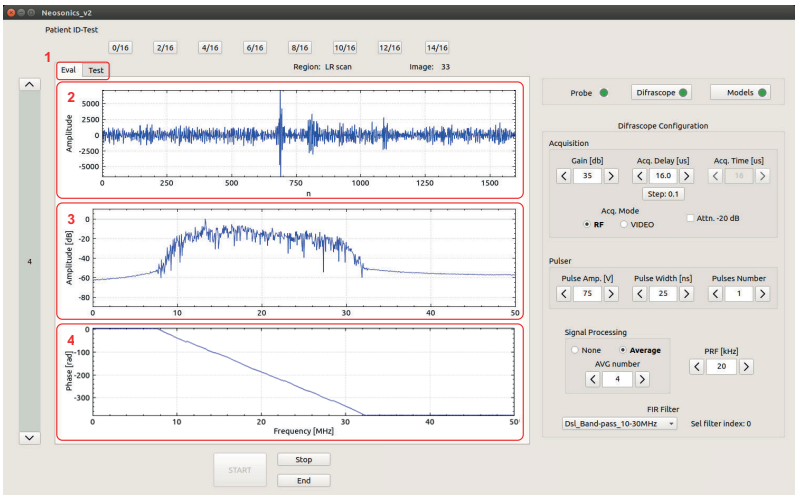


FIGURE A.2: Evaluation view (1) of the application GUI, from where the individual scan lines (A-scans) can be analyzed in the time (2) and frequency domain (magnitude (3) and phase (4)).

Bibliography

[1] *Meningitis: MedlinePlus Medical Encyclopedia*. URL: https://medlineplus.gov/ency/article/000680.htm.

[2] *Meningitis*. URL: https://www.who.int/news-room/fact-sheets/detail/meningitis.

[3] Allan R Tunkel, Diederik van de Beek, and Ws Michael Scheld. "Acute meningitis". In: *Principles and practice of infectious diseases*. Elsevier, 2014, pp. 1097–1138.

[4] Kenadeed Hersi, Francisco J. Gonzalez, and Noah P. Kondamudi. "Meningitis". In: *StatPearls* (Aug. 2023). URL: https://www.ncbi.nlm.nih.gov/books/NBK459360/.

[5] Diederik LH Koelman et al. "Changing epidemiology of bacterial meningitis since introduction of conjugate vaccines: 3 decades of national meningitis surveillance in The Netherlands". In: *Clinical infectious diseases* 73.5 (2021), e1099–e1107.

[6] Joseph Raymond Zunt et al. "Global, regional, and national burden of meningitis, 1990–2016: a systematic analysis for the Global Burden of Disease Study 2016". In: *The Lancet Neurology* 17.12 (2018), pp. 1061–1082.

[7] Chunrun Qu et al. "Global burden and its association with socioeconomic development status of meningitis caused by specific pathogens over the past 30 years: a population-based study". In: *Neuroepidemiology* 57.5 (2023), pp. 316–335.

[8] Allison Portnoy et al. "Estimating costs of care for meningitis infections in low-and middle-income countries". In: *Vaccine* 33 (2015), A240–A247.

[9] Arunava Saha et al. "LUMBAR PUNCTURE IN ACUTE MENINGITIS SYNDROME: DO WE POKE THE SLEEPING BEAR?" In: *CHEST* 164.4 (2023), A1631.

[10] Abdulwahed Zainel, Hana Mitchell, and Manish Sadarangani. "Bacterial meningitis in children: neurological complications, associated risk factors, and prevention". In: *Microorganisms* 9.3 (2021), p. 535.

[11] Michiel van der Flier. "Neonatal meningitis: small babies, big problem". In: *The Lancet Child & Adolescent Health* 5.6 (2021), pp. 386–387.

[12] Nasrin Khalessi and Ladan Afsharkhas. "Neonatal meningitis: risk factors, causes, and neurologic complications". In: *Iranian journal of child neurology* 8.4 (2014), p. 46.

[13] Luis Elvira et al. "Concentration measurement of yeast suspensions using high frequency ultrasound backscattering". In: *Ultrasonics* 64 (2016), pp. 151–161.

[14] Xavier Jimenez et al. "Quantification of very low concentrations of leukocyte suspensions in vitro by high-frequency ultrasound". In: *Ultrasound in Medicine & Biology* 42.7 (2016), pp. 1568–1573.

[15] Luis Elvira et al. "A New Methodology for the Assessment of Very Low Concentrations of Cells in Serous Body Fluids Based on the Count of Ultrasound Echoes Backscattered From Cells". In: *IEEE Transactions on Ultrasonics, Ferroelectrics, and Frequency Control* 68.5 (2020), pp. 1580–1592.

[16] Luis Elvira et al. "Evaluation of the Cell Concentration in Suspensions of Human Leukocytes by Ultrasound Imaging: The Influence of Size Dispersion and Cell Type". In: *Sensors* 23.2 (2023), p. 977.

[17] Jeroen Dudink, Sylke Jeanne Steggerda, and Sandra Horsch. "State-of-the-art neonatal cerebral ultrasound: technique and reporting". In: *Pediatric Research* 87.Suppl 1 (2020), pp. 3–12.

[18] Ginette M Ecury-Goossen et al. "State of the art cranial ultrasound imaging in neonates". In: *JoVE (Journal of Visualized Experiments)* 96 (2015), e52238.

[19] Samuel Pichardo, Vivian W Sin, and Kullervo Hynynen. "Multi-frequency characterization of the speed of sound and attenuation coefficient for longitudinal transmission of freshly excised human skulls". In: *Physics in Medicine & Biology* 56.1 (2010), p. 219.

[20] Hillary R Mount and Sean D Boyle. "Aseptic and bacterial meningitis: evaluation, treatment, and prevention". In: *American family physician* 96.5 (2017), pp. 314–322.

[21] Victoria Poplin, David R Boulware, and Nathan C Bahr. "Methods for rapid diagnosis of meningitis etiology in adults". In: *Biomarkers in medicine* 14.6 (2020), pp. 459–479.

[22] Gwenn Skar et al. "Meningitis in Children: Still a Can't-Miss Diagnosis". In: *Pediatrics in Review* 45.6 (2024), pp. 305–315.

[23] Olaf Hoffman and Joerg R Weber. "Pathophysiology and treatment of bacterial meningitis". In: *Therapeutic advances in neurological disorders* 2.6 (2009), pp. 401–412.

[24] Miguel M Glatstein et al. "Incidence of traumatic lumbar puncture: experience of a large, tertiary care pediatric hospital". In: *Clinical pediatrics* 50.11 (2011), pp. 1005–1009.

[25] Richie Dalai et al. "Is lumbar puncture avoidable in low-risk neonates with suspected sepsis?" In: *American Journal of Perinatology* (2020), pp. 099–105.

[26] Khaled Sadeq Alshaibari et al. "Mothers' views about lumbar puncture for their children in a Maternity and Children's Hospital in Najran, Saudi Arabia". In: *Pediatric Health, Medicine and Therapeutics* (2021), pp. 91–99.

[27] Alyssa Tigner, Sherif A. Ibrahim, and Ian V. Murray. *Histology, White Blood Cell [Last Update: November 14, 2022.]* Jan. 2024. URL: https://www.ncbi.nlm.nih.gov/books/NBK563148/#:~:text=The%20small%20lymphocytes%20are%20similar,more%20cytoplasm%20containing%20azurophilic%20granules..

[28] Ralph E Baddour et al. "High-frequency ultrasound scattering from microspheres and single cells". In: *The Journal of the Acoustical Society of America* 117.2 (2005), pp. 934–943.

[29] Saurav K Shastri et al. "Axial super-resolution in ultrasound imaging with application to non-destructive evaluation". In: *Ultrasonics* 108 (2020), p. 106183.

[30] Alexander Ng and Justiaan Swanevelder. "Resolution in ultrasound imaging". In: *Continuing Education in Anaesthesia, Critical Care & Pain* 11.5 (2011), pp. 186–192.

[31] Robert W Cootney. "Ultrasound imaging: principles and applications in rodent research". In: *ILAR journal* 42.3 (2001), pp. 233–247.

[32] Carmel M Moran and Adrian JW Thomson. "Preclinical ultrasound imaging—a review of techniques and imaging applications". In: *Frontiers in Physics* 8 (2020), p. 124.

[33] Kirsten Christensen-Jeffries et al. "Super-resolution ultrasound imaging". In: *Ultrasound in medicine & biology* 46.4 (2020), pp. 865–891.

[34] Olivier Couture et al. "Microbubble ultrasound super-localization imaging (MUSLI)". In: *2011 IEEE International Ultrasonics Symposium*. IEEE. 2011, pp. 1285–1287.

[35] Olivier Couture et al. "Ultrasound localization microscopy and super-resolution: A state of the art". In: *IEEE transactions on ultrasonics, ferroelectrics, and frequency control* 65.8 (2018), pp. 1304–1320.

[36] Thomas Deffieux, Charlie Demené, and Mickael Tanter. "Functional ultrasound imaging: a new imaging modality for neuroscience". In: *Neuroscience* 474 (2021), pp. 110–121.

[37] Avinoam Bar-Zion et al. "Fast vascular ultrasound imaging with enhanced spatial resolution and background rejection". In: *IEEE transactions on medical imaging* 36.1 (2016), pp. 169–180.

[38] Tali Ilovitsh et al. "Acoustical structured illumination for super-resolution ultrasound imaging". In: *Communications biology* 1.1 (2018), p. 3.

[39] Dmitri V Talapin and Christopher B Murray. "PbSe nanocrystal solids for n-and p-channel thin film field-effect transistors". In: *Science* 310.5745 (2005), pp. 86–89.

[40] Maxime Lanoy et al. "Time reversal sub-wavelength focusing in bubbly media". In: *arXiv preprint arXiv:1510.06911* (2015).

[41] Mathias Fink and Mickael Tanter. "Multiwave imaging and super resolution". In: *Physics today* 63.2 (2010), pp. 28–33.

[42] Michael C Kolios et al. "An investigation of backscatter power spectra from cells, cell pellets and microspheres". In: *IEEE Symposium on Ultrasonics, 2003*. Vol. 1. IEEE. 2003, pp. 752–757.

[43] Ralph E Baddour and Michael C Kolios. "The fluid and elastic nature of nucleated cells: Implications from the cellular backscatter response". In: *The Journal of the Acoustical Society of America* 121.1 (2007), EL16–EL22.

[44] RE Challis et al. "Ultrasound techniques for characterizing colloidal dispersions". In: *Reports on progress in physics* 68.7 (2005), p. 1541.

[45] Aiguo Han et al. "Ultrasonic backscatter coefficient quantitative estimates from high-concentration Chinese hamster ovary cell pellet biophantoms". In: *The Journal of the Acoustical Society of America* 130.6 (2011), pp. 4139–4147.

[46] Show-Huie Chen et al. "Estimation of cell concentration using high-frequency ultrasonic backscattering". In: *J. Med. Biol. Eng* 32.3 (2012), pp. 157–162.

[47] Michiel Postema, Spiros Kotopoulis, and Klaus-Vitold Jenderka. *Physical principles of medical ultrasound*. 2019.

[48] Scott P Grogan and Cristin A Mount. "Ultrasound physics and instrumentation". In: (2021).

[49] John S Mattoon and TG Nyland. "Fundamentals of diagnostic ultrasound". In: *Small Anim Diagnostic Ultrasound Mattoon, 3rd ed.; Mattoon, JS, Nyland, TG, Eds* (2020), pp. 1–49.

[50] Giulio Aniello Santoro, Giuseppe Di Falco, and GA Santoro. "Fundamental principles of ultrasound imaging". In: *Benign Anorectal Diseases: Diagnosis with Endoanal and Endorectal Ultrasound and New Treatment Options* (2006), pp. 3–9.

[51] Didier Vray et al. "Ultrasound medical imaging". In: *Medical Imaging Based on Magnetic Fields and Ultrasounds* (2014), pp. 1–72.

[52] Esperanza Naredo and Indalecio Monteagudo. "Doppler techniques". In: *Clin Exp Rheumatol* 32.1 Suppl 80 (2014), S12–S19.

[53] John E Aldrich. "Basic physics of ultrasound imaging". In: *Critical care medicine* 35.5 (2007), S131–S137.

[54] Pascal Laugier and Guillaume Haïat. "Introduction to the physics of ultrasound". In: *Bone quantitative ultrasound* (2011), pp. 29–45.

[55] *Ultrasound Imaging | FDA*. URL: https://www.fda.gov/radiation-emitting-products/medical-imaging/ultrasound-imaging.

[56] Timothy A Bigelow et al. "The thermal index: its strengths, weaknesses, and proposed improvements". In: *Journal of Ultrasound in Medicine* 30.5 (2011), pp. 714–734.

[57] Christian Kollmann. "Diagnostic ultrasound imaging: inside out". In: *Ultrasound in Medicine and Biology* 41.2 (2015), p. 622.

[58] Vivien Gibbs, David Cole, and Antonio Sassano. *Ultrasound physics and technology: how, why and when*. Elsevier Health Sciences, 2011.

[59] Taner Şen, Omaç Tüfekçioğlu, and Yavuzer Koza. "Mechanical index". In: *Anatolian journal of cardiology* 15.4 (2015), p. 334.

[60] N De Jong. "Mechanical index." In: *European Journal of Echocardiography* 3.1 (2002).

[61] Eberhard Brunner. "Ultrasound system considerations and their impact on front-end components". In: *Analog Devices* 36 (2002), pp. 1–19.

[62] Mohammed Oumer, Ashenafi Tazebew, and Mekuriaw Alemayehu. "Anterior fontanel size among term newborns: a systematic review and meta-analysis". In: *Public Health Reviews* 42 (2021), p. 1604044.

[63] *Dasel Sistemas*. URL: https://www.daselsistemas.com/es/component/content/?id=474&Itemid=890.

[64] *Jetson Nano Brings the Power of Modern AI to Edge Devices | NVIDIA*. URL: https://www.nvidia.com/en-us/autonomous-machines/embedded-systems/jetson-nano/product-development/.

[65] *EDT range of embedded tft display modules*. URL: https://www.lcdtek.co.uk/se-gui-modules/1126-etemb050013adhal-50-smart-embedded-ips-gui-module-425nits-with-ctp.html.

[66] *NVIDIA Deep Learning TensorRT Documentation - - Last updated April 25, 2024*. URL: https://docs.nvidia.com/deeplearning/tensorrt/index.html.

[67] Sara Ajanovic et al. "Non-invasive Meningitis Screening in Neonates and Infants from Spain, Morocco, and Mozambique: a Proof-of-Concept Study [under review]". In: *The Lancet. Infectious Diseases* (2024).

[68] Kaiming He et al. "Deep residual learning for image recognition". In: *Proceedings of the IEEE conference on computer vision and pattern recognition*. 2016, pp. 770–778.

[69] Juan Borrego Carazo. "Efficient Neural Network Inference for Resource Constrained Devices". In: (2022).

[70] John H Lee, Duane S Boning, and Brian W Anthony. "Measuring the absolute concentration of microparticles in suspension using high-frequency B-mode ultrasound imaging". In: *Ultrasound in Medicine & Biology* 44.5 (2018), pp. 1086–1099.

[71] Eric M Strohm et al. "Sizing biological cells using a microfluidic acoustic flow cytometer". In: *Scientific reports* 9.1 (2019), p. 4775.

[72] Luis Elvira et al. "Development and characterization of medical phantoms for ultrasound imaging based on customizable and mouldable polyvinyl alcohol Cryogel–Based materials and 3-D printing: Application to high-frequency cranial ultrasonography in infants". In: *Ultrasound in Medicine & Biology* 45.8 (2019), pp. 2226–2241.

[73] Samuel Dodge and Lina Karam. "Understanding how image quality affects deep neural networks". In: *2016 eighth international conference on quality of multimedia experience (QoMEX)*. IEEE. 2016, pp. 1–6.

[74] Atul Kumar Dwivedi, Subhojit Ghosh, and Narendra D Londhe. "Review and analysis of evolutionary optimization-based techniques for FIR filter design". In: *Circuits, Systems, and Signal Processing* 37 (2018), pp. 4409–4430.